The
Meteoritical
Society

A composite Fe,Ni-FeS and enstatite-forsterite-diopside-glass vitrophyre clast in the Larkman Nunatak 04316 aubrite: Origin by pyroclastic volcanism

Klaus KEIL[1][*], Timothy J. McCOY[2], Lionel WILSON[3,1], Jean-Alix BARRAT[4], Doug RUMBLE[5], Matthias M. M. MEIER[6], Rainer WIELER[6], and Gary R. HUSS[1]

[1]Hawai'i Institute of Geophysics and Planetology, School of Ocean and Earth Science and Technology, University of Hawai'i at Mānoa, Honolulu, Hawai'i 96822, USA
[2]Department of Mineral Sciences, National Museum of Natural History, Smithsonian Institution, Washington, District of Columbia 20560–0119, USA
[3]Lancaster Environment Centre, Lancaster University, Lancaster LA1 4YQ, UK
[4]CNRS UMR 6538 (Domaines Oceaniques), U.B.O.-I.U.E.M., Place Nicolas Copernic, 29280 Plouzane Cedex, France
[5]Geophysical Laboratory, Carnegie Institution of Washington, Washington, District of Columbia 20015–1305, USA
[6]ETH Zürich, Institute of Geochemistry and Petrology, Clausiusstrasse 25, 8092 Zürich, Switzerland
[*]Corresponding author. E-mail: keil@hawaii.edu

Abstract–We studied the mineralogy, petrology, and bulk, trace element, oxygen, and noble gas isotopic compositions of a composite clast approximately 20 mm in diameter discovered in the Larkman Nunatak (LAR) 04316 aubrite regolith breccia. The clast consists of two lithologies: One is a quench-textured intergrowth of troilite with spottily zoned metallic Fe,Ni which forms a dendritic or cellular structure. The approximately 30 μm spacings between the Fe,Ni arms yield an estimated cooling rate of this lithology of approximately 25–30 °C s^{-1}. The other is a quench-textured enstatite-forsterite-diopside-glass vitrophyre lithology. The composition of the clast suggests that it formed at an exceptionally high degree of partial melting, perhaps approaching complete melting, and that the melts from which the composite clast crystallized were quenched from a temperature of approximately 1380–1400 °C at a rate of approximately 25–30 °C s^{-1}. The association of the two lithologies in a composite clast allows, for the first time, an estimation of the cooling rate of a silicate vitrophyre in an aubrite of approximately 25–30 °C s^{-1}. While we cannot completely rule out an impact origin of the clast, we present what we consider is very strong evidence that this composite clast is one of the elusive pyroclasts produced during pyroclastic volcanism on the aubrite parent body (Wilson and Keil 1991). We further suggest that this clast was not ejected into space but retained on the aubrite parent body by virtue of the relatively large size of the clast of approximately 20 mm. Our modeling, taking into account the size of the clast, suggests that the aubrite parent body must have been between approximately 40 and 100 km in diameter, and that the melt from which the clast crystallized must have contained an estimated maximum range of allowed volatile mass fractions between approximately 500 and approximately 4500 ppm.

INTRODUCTION

The aubrites, or enstatite achondrites, are nearly monomineralic enstatite pyroxenites. They consist of dominant and nearly FeO-free enstatite and contain minor, generally albitic plagioclase, nearly FeO-free diopside and forsterite, Si-bearing metallic Fe,Ni (usually

kamacite), Ti-Cr-bearing troilite, and a large number of rare accessory minerals, many unknown from Earth, which formed under highly reducing conditions (e.g., Keil 1989). The aubrites are igneous rocks, many brecciated, that are thought to have been formed by the melting, fractionation, and differentiation of enstatite chondrite-like precursor lithologies, as is likely in view of

1719

the compositional and isotopic similarities of aubrites and enstatite chondrites (e.g., Keil 2010). One long-standing problem of aubrite genesis has been the lack of enstatite-plagioclase (basaltic) rocks in the world's meteorite collections, rocks complementary to the enstatite-rich aubrites. These must have formed during partial melting, if the precursor lithology was enstatite chondrite-like (note that enstatite chondrites contain approximately 10% albitic plagioclase; Mason 1966; Keil 1968).

To explain the lack of enstatite-plagioclase basalts, Wilson and Keil (1991) calculated that if the enstatite-plagioclase basaltic partial melts contained a few hundred to thousands ppm of volatiles, as is likely based on the degassing measurements of enstatite chondrites by Muenow et al. (1992), then these melts, as they approached the surface of a small, low-gravity body less than about 100 km in radius, would disrupt into a spray of pyroclasts from approximately 30 µm to approximately 4 mm in size (Wilson and Keil 1996). These pyroclasts would move faster than the escape velocity of the body and, thus, these melts would escape into space during the very early history of the solar system and be lost by collisions with the forming planets and by spiraling into the Sun.

Samples of these pyroclasts have therefore proven elusive, compromising our ability to fully understand their formation. Recently, however, McCoy and Gale (2006) suggested that two unusual, 10 mm-sized joined clasts, which we interpret to be a single, composite clast, in the Larkman Nunatak (LAR) 04316 aubrite, a regolith breccia originally of mass 1163 g, may be remnants from the pyroclastic volcanism proposed by Wilson and Keil (1991). They describe one as a quench-textured Fe,Ni-FeS clast of a type previously unknown from aubrites, and the other as a silicate vitrophyre composed of enstatite-forsterite-glass, and they noted that the two clasts are joined by an igneous contact (Fig. 1). They also suggested that the vitrophyre may be a sample of the elusive basaltic partial melt that formed during the melting of the precursor lithology of the aubrites and, possibly because of its large size, did not escape into space during pyroclastic volcanism but, instead, fell back onto the aubrite parent body. They also pointed out that this rock is somewhat similar in composition and mineralogy to the three rare (and smaller) clasts described by Fogel (2005) as remnants of the missing basaltic melts (and named by him "aubrite basalt vitrophyres," or ABVs).

Herein we present detailed mineralogic, petrologic, chemical, and isotopic studies of the LAR 04316 host and of what we interpret to be a single, approximately 20 mm-sized, composite clast consisting of two separate and distinct immiscible lithologies, the Fe,Ni-FeS and
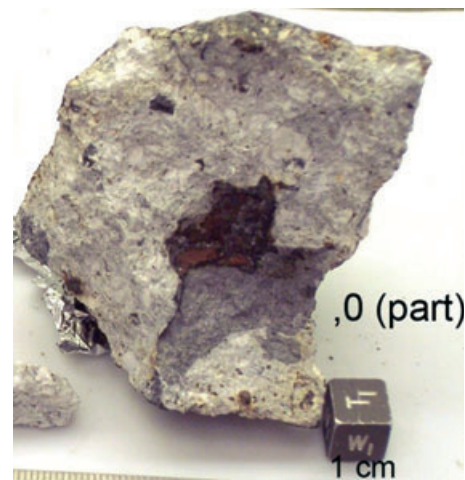

Fig. 1. Photograph of the main mass of the LAR 04316 aubrite. It contains a clast approximately 20 mm in diameter, embedded in the light grayish-white matrix of this solar gas-bearing regolith breccia. The clast consists of a black, Fe,Ni-FeS lithology (upper part) and a gray, enstatite-forsterite-diopside-glass (basaltic) vitrophyre lithology (lower part). Photo courtesy of the Meteorite Processing Laboratory at NASA's L.B. Johnson Space Center, Houston, TX.

the enstatite-forsterite-diopside-glass lithologies. We suggest that this object formed by simultaneous migration of a batch of immiscible Fe,Ni-FeS and silicate partial melts upward to the surface of the aubrite parent body and disruption of these melts into droplets by shear forces or gas bubble expansion when reaching the surface during an episode of pyroclastic volcanism, and that it did not escape into space but fell back onto the aubrite parent body because of its unusually large size, as previously suggested by McCoy and Gale (2006).

ANALYTICAL TECHNIQUES AND SAMPLES

A polished thin section of the host aubrite (LAR 04316,7) and of the vitrophyre (LAR 04316,4), and a polished section of the Fe,Ni-FeS lithology (LAR 04316,3) were studied with an optical petrographic microscope in transmitted and reflected light. Mineral constituents were surveyed in backscattered and secondary electrons in a JEOL 5900 LV scanning electron microscope (SEM) at the Hawai'i Institute of Geophysics and Planetology, operated at 15 keV accelerating potential. The Thermo Electron NanoTrace energy dispersive detector (EDS) of the SEM was used to identify and semiquantitatively analyze mineral constituents. A JEOL JXA 8200F fully automated electron probe microanalyzer (EPMA) in the Department of Geology and Geophysics of the University of Hawai'i at Mānoa was used to map portions of the polished thin sections in backscattered electrons and X-rays. These
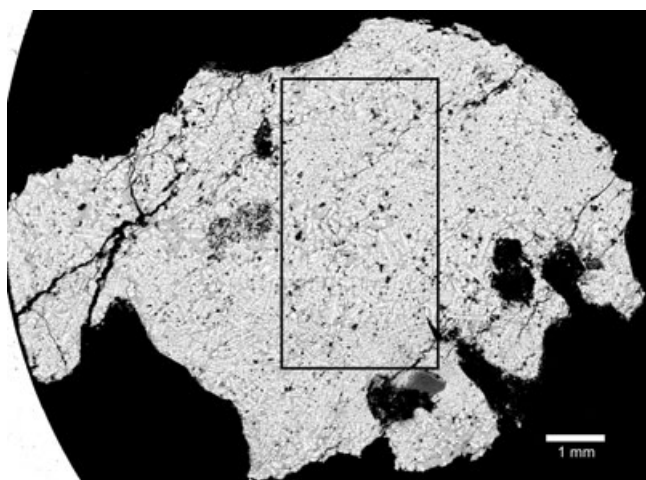
Fig. 2. Backscattered electron (BSE) image of the Fe,Ni-FeS lithology LAR 04316,3 obtained in the SEM and mosaiced with NORAN software. It shows the quench texture of the metallic Fe,Ni dendrites (white) with arm/cell spacings of approximately 30 μm, embedded in troilite (gray). Black in the rectangular area are cracks and holes in the section; outside the rectangular area, black are holes, an alabandite inclusion, (gray, lower center; see also Fig. 9) and the surrounding epoxy of the section. The outlined approximately 2.4 × 4.6 mm rectangular area, shown magnified in Fig. 3, was used to determine the vol% of Fe,Ni and FeS in the lithology.
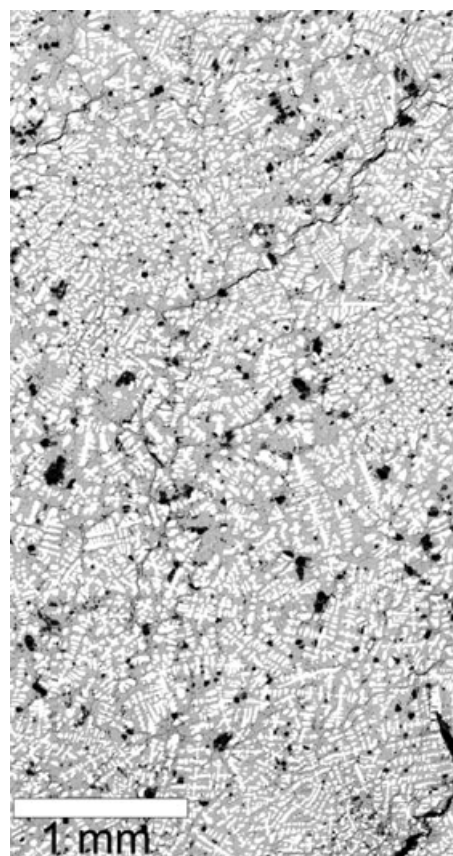

Fig. 3. Enlarged BSE image of the rectangular area outlined in Fig. 2 of the Fe,Ni-FeS lithology LAR 04316,3, showing the quench texture of the metallic Fe,Ni dendrites (white) with arm/cell spacings of approximately 30 μm, embedded in troilite (gray). This area was used for the determination of the modal content of metallic Fe,Ni, and troilite and was selected for modal analysis because it has relatively few holes and cracks (black).

maps were used to locate minerals to be subjected to quantitative elemental analysis, and to illustrate the complex textures of the different lithologies of the clast. The EPMA was operated at 15 keV for silicates and interstitial material in the vitrophyre, and 20 keV for sulfides and metallic Fe,Ni. The X-ray scanning images were obtained with an electron beam of 15 keV accelerating potential and 25 nA current. The bulk composition of a vein cutting across the enstatite inclusion within the vitrophyre was determined using a 15 keV broad electron beam approximately 5 μm in diameter. Natural and synthetic standards of well-known compositions were used for quantitative analysis, and data were corrected for differential matrix effects using the company-supplied software.

A backscattered electron (BSE) image map of an approximately 2.4 × 4.6 mm portion of the Fe,Ni-FeS lithology (Figs. 2 and 3) relatively free of cracks and voids (black) was obtained in the SEM and mosaiced with NORAN software. This image was used to determine the vol% of Fe,Ni and FeS, and these data were converted into wt% using a density of 7900 kg m^{-3} for metallic Fe,Ni and 4750 kg m^{-3} for troilite. Minor cracks and voids in the section encountered during modal analysis were deducted from the total, and the mode was calculated for Fe,Ni and FeS on a crack- and void-free basis. Modal abundances were determined with

Multispec image data analysis software (Biehl and Landgrebe 2002). Digital point counting techniques were similar to those used by others (e.g., Hicks 2002; Maloy and Treiman 2007; Van Niekerk et al. 2007). The mosaiced maps mismatched slightly at some boundaries and produced minor image duplication. It was not possible to correct for this, but it appears that the net effect simply was to make the section image larger, thus we assume that the Fe,Ni and FeS proportions retained their representative modal abundances. A compiled map of the approximately 2.4 × 4.6 mm area was imported into Multispec, and a supervised classification map with point counting statistics was produced using a Minimum Euclidean Distance algorithm. The final thematic classified map was visually compared with the equivalent portion of the BSE image to ensure that Fe,Ni and FeS were classified accurately (i.e., thematic accuracy). The class training had a statistical overall

performance of 98.8%. Based on this we assign an uncertainty of $\pm 1.2\%$ to the results.

Major, minor, and trace element abundances of the vitrophyre (subsample "18" of approximately 150 mg) and the host aubrite (subsample "40" of approximately 2 g) were obtained by powdering the samples in a boron carbide mortar and pestle. Major elements, Cr and Ni were determined at the Université de Bretagne Occidentale, Brest, France, by ICP-AES (inductively coupled plasma-atomic emission spectrometry) using the procedure of Cotten et al. (1995). The accuracy of these measurements is better than 5%, and the reproducibility is better than 3%. Trace element concentrations were measured at the Institut Universitaire Européen de la Mer (IUEM), Plouzané, France, by ICP-MS (inductively coupled plasma–mass spectrometry) using a Thermo Element 2 spectrometer following the procedure of Barrat et al. (2007). Based on standard measurements and sample duplicates, trace element concentration reproducibility is generally better than 5%, except for W, which is generally better than 10%.

Oxygen isotopic analyses were made on aliquots of the aubrite host (subsample "45") and vitrophyre (subsample "47"). Samples were prepared by crushing in a boron nitride mortar and pestle, ultrasonicating in diluted HCl, washing in distilled water, drying, and removing magnetic material before analysis. Samples contained a range of grain sizes and, in the case of the aubrite host, cleavage fragments of enstatite were up to one millimeter in length. Samples were loaded in a reaction chamber (Sharp 1990) and repeatedly reacted with BrF_5 at room temperature until their oxygen blank was below detection. Samples were heated under 30 torr of BrF_5 with a Synrad 30 watt CO_2 laser at 10.6 μm wavelength to release O_2 quantitatively for analysis (Rumble and Hoering 1994). Aliquots of Gore Mountain garnet (USNM 107144, obtained courtesy of J. Post, Smithsonian Institution) were analyzed during each analytical session. The reference garnet gives a value of $\delta^{18}O_{VSMOW}$ of 6.0‰ in comparison to UWG-2 (Valley et al. 1995; Rumble et al. 1997). The two σ standard deviations of repeated analyses of USNM 107144 garnet were $\Delta^{17}O \pm 0.03$, $\delta^{17}O \pm 0.09$, and $\delta^{18}O \pm 0.17\%$. The value used for the slope of the Terrestrial Fractionation Line (TFL) is 0.526 (± 0.001) (Rumble et al. 2007).

In an attempt to determine the age of the Fe,Ni-FeS lithology, we used the CAMECA ims 1280 ion microprobe in the W.M. Keck Cosmochemistry Laboratory at the University of Hawai'i at Mānoa (HIGP) to analyze the troilite for the possible presence of ^{60}Ni from the decay of short-lived ^{60}Fe. For each measurement cycle, ^{60}Ni, ^{61}Ni, and ^{62}Ni were measured simultaneously on three electron multipliers, followed by a field switch to put ^{57}Fe on a Faraday cup. A mass resolving power of approximately 7500 was used, which is sufficient to resolve all significant interferences, including $^{60}NiH^+$ on $^{61}Ni^+$.

The concentrations of the cosmogenic radionuclides ^{10}Be and ^{26}Al in the aubrite host were determined by K. Welten (personal communication, 2009) at the Space Science Laboratory, University of California, Berkeley, using techniques and procedures described by Welten et al. (2006).

The noble gas (He, Ne, Ar) inventory was measured at the ETH Zürich noble gas laboratory, using a sector field noble gas mass spectrometer (Graf et al.1990). A sample of the aubrite host, subsample "42" was wrapped in aluminum foil and noble gases were extracted by a single-step heating to 1800 °C. Ar was separated from He and Ne using charcoal cooled with liquid nitrogen. The He-Ne and Ar were then measured separately in sequence. Interferences on masses 20 ($^{40}Ar^{++}$, $H_2^{18}O^+$) and 22 (CO_2^{++}) were corrected for, although the corrections were significantly smaller than the errors from ion counting statistics. The sample gas was calibrated using a bottle standard of atmospheric composition (Heber et al. 2009).

RESULTS

As noted by McCoy and Gale (2006), the boundary between the Fe,Ni-FeS and the vitrophyre lithology is igneous, i.e., the two immiscible melts were in contact as they formed and cooled and crystallized simultaneously. This is apparent from the hand specimen image (Fig. 1), and is also indicated by the fact that the vitrophyre contains several smaller Fe,Ni-FeS clasts and inclusions of very similar texture to the large Fe,Ni-FeS lithology. One of these is approximately 1500 μm in longest dimension (Fig. 11) and occurs on the boundary of the vitrophyre and the brecciated aubrite host portion and actually is partly included in the vitrophyre, whereas other, smaller clasts occur totally embedded in the vitrophyre within the plane of the thin section and in an enstatite inclusion within the vitrophyre (Fig. 13; see below). Thus, the Fe,Ni-FeS and silicate vitrophyre lithologies constitute one single, composite clast.

Mineralogy, Petrology, Bulk Chemical and Oxygen Isotope Compositions of the Aubrite Host

The average oxygen isotope composition of the aubrite host, LAR 04316,45, $\delta^{18}O = 4.53\%$, $\delta^{17}O = 2.37\%$, and $\Delta^{17}O = -0.01\%$, lies within the range of aubrite and EH chondrite compositions reported by Clayton and Mayeda (1996), Newton et al. (2000) and Miura et al. (2007) (Fig. 4) and, thus, confirms the classification of the rock as an aubrite. The uncertainty in $\Delta^{17}O$ for LAR 04316,45, 0.03‰, is the same as that of reference material USNM 107144. The uncertainties in $\delta^{18}O$ and $\delta^{17}O$, $\pm 0.42\%$ and
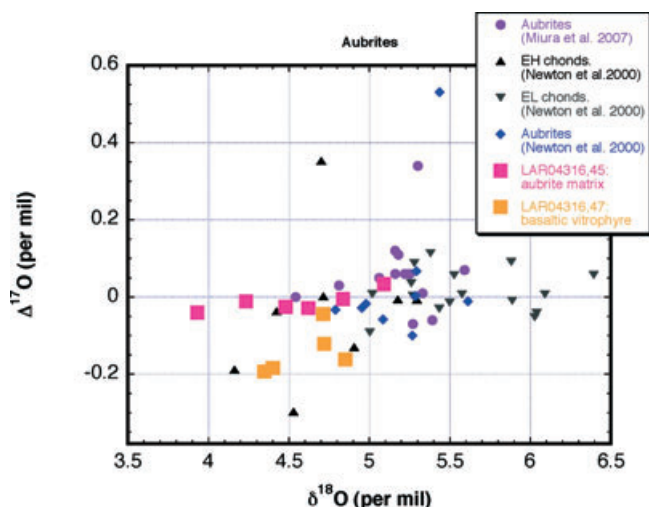
Fig. 4. Oxygen isotope compositions of $\delta^{18}O$ versus $\Delta^{17}O$ for the aubrite host LAR 04316 (subsample ''45'' herein named aubrite matrix), and the enstatite-forsterite-diopside-glass vitrophyre LAR 04316 (subsample ''47'' herein named basaltic vitrophyre), compared with published oxygen isotopic analyses of aubrites and enstatite chondrites.

0.24‰, respectively, are larger than the uncertainties measured concurrently for reference material USNM 107144. Aliquots of 2 mg of aubrite host were drawn for analysis from a population of enstatite cleavage fragments as large as 1 mm in length. Results of a single analysis were dominated by contributions from a few grains. The observed dispersion in $\delta^{18}O$ and $\delta^{17}O$ values may reflect heterogeneity in $\delta^{18}O$ and $\delta^{17}O$, but not $\Delta^{17}O$. Alternatively, the dispersion in δ-values may be an analytical artifact encountered in the analysis of Mg-rich silicate minerals with the laser fluorination technique. Because of its nearly mono-mineralic, $MgSiO_3$ composition, the aubrite host is a difficult analytical target. During laser fluorination of enstatite, a virtually pure MgF_2 molten globule envelopes unreacted silicate, armoring against stoichiometric recovery of total oxygen. The difficulty of ensuring complete fluorination of all residual silicate gives rise to discrepancies in $\delta^{17}O$ and $\delta^{18}O$ values but has a smaller impact on $\Delta^{17}O$ values.

The noble gas (He, Ne, Ar) inventory of a sample of the aubrite host, subsample ''42'' is shown in Table 1. The reported decomposition into trapped and cosmogenic components is based on standard assumptions for isotopic compositions of cosmogenic and trapped solar wind endmembers (see also contents in the second to next paragraph), and an estimated contribution of radiogenic ^4He of 1000×10^{-8} ccSTP g^{-1}. Trapped Ne is not abundant enough to unequivocally prove that it has a solar-like isotopic composition. However, $^4He/^{20}Ne$ and $^{20}Ne/^{36}Ar$ ratios of the trapped component are only slightly below solar-wind values (Heber et al. 2009) as is

Table 1. Measured noble gas concentrations.

Measured amounts, in 10^{-8} ccSTP g^{-1}				
^3He	^4He			
111.3±0.3	33600±1800			
^{20}Ne	^{21}Ne	^{22}Ne		
158.0±0.4	31.9±0.1	44.0±0.1		
^{36}Ar	^{38}Ar	^{40}Ar		
4.04±0.00	1.19±0.00	1337±45		
Cosmogenic component, in 10^{-8} ccSTP g^{-1}				
$^3He_{cos}$	$^{21}Ne_{cos}$	$^{38}Ar_{cos}$	$^3He/^{21}Ne_{cos}$	$^{22}Ne/^{21}Ne_{cos}$
96.7	31.6	1.19	3.04	1.06±0.02
P3	P21	P38		
2.31	0.618	0.0238		
T3	T21	T38		
> 41.6	> 51.0	>49.7		
Trapped component, in 10^{-8} ccSTP g^{-1}				
^4He	^{20}Ne		$^4He/^{20}Ne$	
32000	129		248	

All gas amounts in 10^{-8} ccSTP g^{-1}, (1 ccSTP = 2.687 $\times 10^{19}$ atoms), of the aubrite host, subsample ''42'' (31.4 mg). A radiogenic ^4He concentration typical of aubrites, of approximately 1000×10^{-8} ccSTP g^{-1}, was assumed. Trapped and cosmogenic components calculated as described in the text. Maximal production rates (P3, P21, P38; in 10^{-8} ccSTP g^{-1}/Ma) calculated according to Leya and Masarik (2009) for an object with radius = 40 cm, and sample shielding depth of approximately 30 cm (see text). Resulting exposure ages (T3, T21, T38; in Ma) have to be considered as minimum ages, because the preatmospheric meteorite could also have been larger than assumed here. Errors on measured concentrations include only ion counting statistics, which due to rounding to the least significant digit may result in errors displayed as ''±0.00'' if the error is smaller than ±0.005. However, calibration variability is an additional source of error: approximately 1% for amounts of He, Ne and 3% for amounts of Ar.

typically observed in other solar-gas-rich meteorites (e.g., Wieler et al. 1989). This proves that LAR 04316 is a regolith breccia, similar to aubrites such as Pesyanoe and Khor Temiki (Gerling and Levskii 1956; Eberhardt et al. 1965). The calculated concentrations of cosmogenic ^3He, ^{21}Ne, and ^{36}Ar allow the determination of a consistent cosmic-ray exposure age (Table 1 and below).

Study of polished thin section LAR 04316,7 in the optical microscope and in backscattered electron and X-ray images shows that the aubrite host has the typical cataclastic texture and mineralogy of a regolith breccia. The rock consists mostly of enstatite fragments ranging from dust-fine material up to approximately 3000 μm in longest dimension. Minor shock veins consisting of crushed, very fine-grained enstatite were noted in the optical microscope due to their nearly

Table 2. Average electron microprobe analyses of silicate minerals in the LAR host aubrite (H), the enstatite-forsterite-diopside-glass vitrophyre (V), and the enstatite inclusion (I) and its melt vein (M-V) within the vitrophyre (in wt%, endmembers in mole%).

	H	H	V	V	V	V	I	M-V in I	M-V in I	M-V in I
	En	Di	En	Fo	Di	G	En	En	Fo	Bulk
N	11	7	8	10	1	4	4	1	1	7
SiO_2	59.8	55.5	60.2	42.9	56.1	76.2	60.4	60.0	42.9	67.3
TiO_2	n.d.	n.d.	b.d.	n.d.	0.23	0.22	n.d.	n.d.	n.d.	0.35
Al_2O_3	0.11	0.43	0.20	b.d.	0.41	8.3	0.06	0.12	0.03	9.2
FeO	0.05	0.02	1.67	1.91	0.03	2.76	0.23	1.20	0.88	2.29
MnO	0.07	n.d.	0.24	0.17	0.05	0.41	0.11	0.31	0.24	0.95
MgO	39.8	21.4	38.4	55.7	21.8	4.9	39.7	38.8	56.6	8.4
CaO	0.60	22.4	0.16	0.07	22.5	5.7	0.34	0.16	0.08	9.5
Na_2O	b.d.	0.21	b.d.	b.d.	0.22	2.14	b.d.	b.d.	b.d.	0.41
K_2O	n.d.	n.d.	b.d.	n.d.	b.d.	0.36	n.d.	n.d.	n.d.	0.39
S	n.d.	n.d.	b.d.	n.d.	n.d.	0.19	n.d.	n.d.	n.d.	0.19
Total	100.43	99.96	100.87	100.75	101.34	101.18	100.84	100.59	100.73	98.71
Wo	1.06	42.93	0.29		42.58		0.62	0.30		
En	98.86	57.04	97.33		57.38		99.06	98.0		
Fs	0.07	0.03	2.37		0.04		0.33	1.70		
Fo				98.4					99.04	
Fa				1.88					0.86	

Notes: N = number of analyses; b.d. = below detection; n.d. = not determined; En = enstatite; Di = diopside; Fo = forsterite; G = glass.

opaque appearance in transmitted light as a result of their fine grain size. Forsterite was not encountered during our electron microprobe analyses, but a few tiny grains were observed in the optical microscope and in X-ray scanning images, and diopside is sparse and heterogeneously distributed, but several large grains were found. The largest is 1100 μm in longest dimension and has a maximum width of approximately 100 μm. The second largest grain is approximately 500 μm in longest dimension and approximately 100 μm in width. Compositionally, diopside ($Wo_{42.9}En_{57.1}Fs_{<0.1}$) contains minor amounts of Al_2O_3 (0.43) and Na_2O (0.21), is nearly FeO free (0.02) (all in wt%), and is rather homogeneous; of the seven analyses averaged in Table 2, four are from the 500 μm-sized grain and three are from the largest grain of 1100 μm in longest dimension. Fe,Ni and troilite are very sparse, and very rarely daubreelite is associated with accessory troilite in places and occurs as exsolution lamellae in it, together with very minor alabandite. No oldhamite was observed in the thin sections studied herein. The mineral compositions are typical for aubrites: Enstatite ($Fs_{0.07}$), and diopside ($Fs_{0.03}$) are nearly FeO free (Table 2). Troilite is nearly stoichiometric FeS, but contains minor Ti (approximately 0.9), Cr (approximately 0.8) and Mn (approximately 0.05), and daubreelite contains minor Mn (approximately 1.9), Ti (approximately 0.09), and Mg (approximately 0.09) (Table 3). Alabandite is the most Mn-rich known from aubrites, with only approximately 8.8 Fe, in addition to approximately 1.1 Cr, approximately 0.05 Ti, approximately 0.3 Mg, and approximately 0.05 Ca (Table 3; Fig. 5). Metallic Fe,Ni is unusual in composition and has only approximately 2.5 Ni and 0.26 Co. The analyzed grains are very small, at most approximately 80 μm in longest dimension, so the low contents of S (0.05), P (0.09), and Si (0.13; all in wt%) are somewhat uncertain (Table 3).

Cosmogenic [10]Be and [26]Al in the aubrite host ([10]Be: 18.3 ± 0.4 dpm kg^{-1}; [26]Al: 42 ± 1 dpm kg^{-1}; K. Welten, personal communication) are similar to typical saturation values for stony meteorites. This indicates that this aubrite was exposed as a small object in space for more than about four half-lives of [10]Be, i.e., more than approximately 5 Ma. A better constrained minimum cosmic-ray exposure age can be derived from the cosmogenic component of the He, Ne, and Ar inventory measured in sample LAR 04316,42. The [22]Ne/[21]Ne ratio of cosmogenic Ne and the cosmogenic [3]He/[21]Ne ratio can be used as an indicator of shielding depth during cosmic-ray irradiation (Table 1). The relatively large uncertainty of ($^{22}Ne/^{21}Ne)_{cos}$ is due to the correction necessary for trapped Ne of solar-like composition (with an assumed $^{20}Ne/^{22}Ne$ ratio of 11.8–13.2 which covers the range observed for most meteorites with solar-like gases). We use the model of Leya and Masarik (2009) to constrain the shielding depth of our sample. The smallest object of aubrite chemistry fitting the observed ratios has a preatmospheric radius of 20 cm, with the samples originating from approximately 10 cm below the surface, but the object could well have been considerably larger,

Table 3. Average electron microprobe analyses of sulfides (Tr = troilite; D = daubreelite; Al = alabandite) and metallic Fe,Ni (Fe) in the LAR aubrite host, of Ni-rich (Ni-r), Ni-poor (Ni-p), and zoned metallic Fe,Ni (Fe-z) in the Fe,Ni-FeS lithology (L-1), and of troilite, keilite (K), and alabandite in the alabandite-keilite inclusion (I) in the Fe,Ni-FeS lithology shown in Fig. 9 (in wt%).

	H Tr	H D	H Al	H Fe	L-1 Ni-r	L-1 Ni-p	L-1 Fe-z	I Tr	I K	I Al
N	120	25	4	12	3	8	5	7	9	15
Fe	61.8	18.0	8.8	96.7	64.2	91.1	76.9 (73.5–82.7)	62.6	36.4	19.5
Mn	0.05	1.87	52.0	n.d.	n.d.	n.d.	n.d.	1.08	23.4	40.0
Cr	0.84	34.4	1.13	n.d.	n.d.	n.d.	n.d.	0.88	0.85	0.45
Ti	0.93	0.11	0.05	n.d.	n.d.	n.d.	n.d.	<0.01	<0.01	0.02
Mg	0.12	0.09	0.29	n.d.	n.d.	n.d.	n.d.	<0.01	1.93	2.26
Ca	b.d.	b.d.	0.05	n.d.	n.d.	n.d.	n.d.	b.d.	0.35	0.26
S	36.7	43.7	36.5	0.05	0.36	0.19	0.20 (0.12–0.30)	36.8	37.7	38.1
Ni	n.d.	n.d.	n.d.	2.49	32.8	7.53	20.6 (14.9–24.2)	n.d.	n.d.	n.d.
Co	n.d.	n.d.	n.d.	0.26	0.49	0.47	0.55 (0.54–0.56)	n.d.	n.d.	n.d.
Si	n.d.	n.d.	n.d.	0.13	b.d.	b.d.	b.d.	n.d.	n.d.	n.d.
P	n.d.	n.d.	n.d.	0.09	0.29	0.28	0.50 (0.45–0.54)	n.d.	n.d.	n.d.
Total	100.44	98.17	98.82	99.72	98.14	99.58	98.75	101.36	100.63	100.33

Notes: N = number of analyses; b.d. = below detection; n.d. = not determined.

as is suggested by the Ar data (see end of this paragraph). As the production rates for larger objects are smaller, the exposure ages reported herein are minimum exposure ages. The highest production rates for ^{3}He, ^{21}Ne, and ^{38}Ar occur at 30 cm shielding in an object of 40 cm radius. The corresponding minimum exposure ages are 41.6, 51.0, and 49.7 Ma, respectively. This is in the range of approximately 12–127 Ma of published exposure ages for aubrites and coincident with the proposed cluster at approximately 50 Ma (Eugster 2003; Lorenzetti et al. 2003), but as these are minimum ages, such an attribution can only be tentative. The approximately 18% lower ^{3}He age is explained by He loss, almost exactly matching the difference between the measured ^{3}He/^{21}Ne (3.04) and the ratio predicted from the model (3.75) for these shielding conditions (approximately 19%). Note also that the Ar exposure age is calculated based on the assumption that all ^{38}Ar is cosmogenic. A deconvolution of trapped (^{36}Ar/^{38}Ar = 5.35) and cosmogenic (^{36}Ar/^{38}Ar = 0.65) endmembers yields a ^{38}Ar exposure age that is significantly lower than the ^{21}Ne exposure age. Assuming all ^{38}Ar to be cosmogenic, the excess of approximately 3.3 × 10^{-8} ccSTP g^{-1} of ^{36}Ar can be attributed to neutron-capture Ar, a value similar to the one observed in the Shallowater aubrite (Bogard et al. 1995). As neutron-capture is only important in larger objects (greater than approximately 1 m diameter; e.g., Wieler 2002), the observation of neutron-capture ^{36}Ar might imply a large preatmospheric size and an exposure age in excess of the values listed herein.

We have determined the major and trace element abundances in the aubrite host (Tables 4, 5). Not surprisingly, its major element concentrations are strongly controlled by the composition of the orthopyroxene, in agreement with its nearly mono-mineralic nature. The chondrite-normalized rare earth element (REE) pattern (Fig. 6B) is slightly bow-shaped (La$_n$/Sm$_n$ = 0.64; Gd$_n$/Lu$_n$ = 1.22), with a marked negative Eu anomaly (Eu/Eu* = 0.50). REE abundances are relatively high for aubrites, approaching chondritic values.

Mineralogy, Petrology, and Bulk Composition of the Fe,Ni-FeS Lithology

Study of section LAR 04316,3 shows that this quench-textured lithology consists of troilite that is intergrown with spottily zoned metallic Fe,Ni which forms a dendritic or cellular structure with arm/cell spacings of approximately 30 μm (Fig. 7). Such lithologies have not previously been known from aubrites, but similar metallic Fe,Ni-FeS assemblages have been described as spheres from around Meteor Crater, Arizona and from lunar soils, as well as from iron meteorites and from clasts in chondritic meteorite breccias (e.g., Blau et al. 1973; Blau and Goldstein 1975; Scott 1982). Experiments with metal-sulfide mixtures by Flemings et al. (1970) and Blau and Goldstein (1975) have shown that the spacings between the dendrite arms decrease with increasing cooling rate and, thus, a cooling rate estimate can be obtained for the Fe,Ni-FeS lithology in LAR 04316. Based on the approximately 30 μm spacing between the Fe,Ni arms, Fig. 8 yields an estimated cooling rate of the lithology of approximately 25–30 °C s^{-1}, as previously suggested by McCoy and Gale (2006).

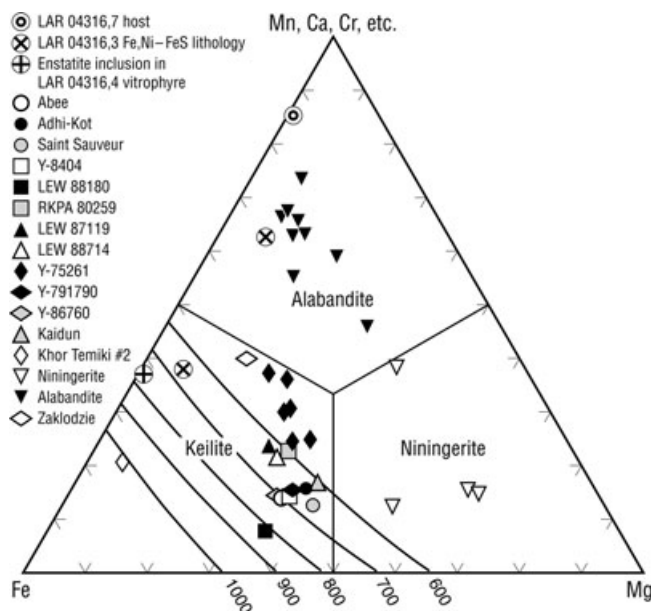The modal Fe,Ni and troilite contents of an approximately 2.4 × 4.6 mm portion of the lithology

Fig. 5. Average electron microprobe analyses of Fe-rich/Mg-poor alabandite from the LAR 04316,7 host (Table 3), of troilite, alabandite, and keilite from the inclusion in the LAR 04316,3 Fe,Ni-FeS lithology (Table 3; Fig. 9), and of keilite from a metallic Fe,Ni-troilite-keilite globule in the enstatite inclusion within the vitrophyre LAR 04316,4 (Table 3; Fig. 13A), plotted in a ternary diagram in terms of atom% on the basis of 1 S for the endmembers Fe, Mg, and Mn + Ca + Cr (following the custom of Shimizu et al. 2002). Also plotted for comparison are literature analyses for keilite, alabandite, and niningerite (Keil 2007). The ternary solvus lines for five temperatures (in °C) are after Skinner and Luce (1971) and were experimentally determined for the system FeS-MgS-MnS, indicating that the minimum formation temperatures of keilite in the inclusion in the Fe,Ni-FeS lithology LAR 04316,3 were approximately 660 °C, and for keilite in the enstatite inclusion within the vitrophyre LAR 04316,4 approximately 770 °C. Modified from Keil (2007) and reprinted with permission from Elsevier.

Table 4. Major element (in wt%; by ICP-AES) abundances in the enstatite-forsterite-diopside-glass vitrophyre lithology (subsample "18") from the LAR 04316 aubrite, and of the host LAR 04316 aubrite (subsample "40"), compared to the bulk composition of aubrites (after Watters and Prinz [1979], as modified by Keil [2010]).

Oxides	LAR 04316,18	LAR 04316,40	Bulk aubrites
SiO$_2$	56.1[a]	56.5[a]	58.5
TiO$_2$	0.08	0.05	0.05
Al$_2$O$_3$	1.79	0.91	0.8
Cr$_2$O$_3$	0.19	0.09	0.03
FeO	3.48	1.37	0.05
MnO	0.33	0.28	0.04
MgO	35.40	39.19	38.1
CaO	1.70	1.17	0.94
Na$_2$O	0.8	0.43	0.41
K$_2$O	0.1	0.04	0.02
P$_2$O$_5$	0.01	0.01	n.d.
CIPW norm, in wt%			
Pl	7.77	4.07	3.78
Or	0.59	0.24	0.12
Di	5.78	4.15	3.38
En	69.22	74.06	88.26
Fo	16.45	17.13	4.34
Il	0.15	0.1	0.09
Ap	0.02	0.02	0.02

[a]SiO$_2$ abundances in the two LAR samples were estimated by difference to 100%. Note that the normative plagioclase/orthoclase component of 8.36 wt% in LAR 04316,18 is present in the interstitial mesostasis (glass), and that there is no ilmenite and apatite in this rock nor the bulk aubrites; TiO$_2$ is probably present as Ti in trace FeS, and P$_2$O$_5$ may be present in trace metallic Fe,Ni. Also, the high normative Fo value for the host aubrite of 17.13% is unrealistic, as microscopic study of the host aubrite shows only traces of forsterite.

relatively free of voids and cracks (Figs. 2 and 3) were determined to be 43 vol% Fe,Ni and 57 vol% FeS. Using approximate mineral densities, these vol% were converted to wt%, yielding 56.6 wt% Fe,Ni and 43.4 wt% FeS. This is similar to the approximately 50 wt% Fe,Ni and approximately 50 wt% FeS estimates given by McCoy and Gale (2006).

The zoning of the metallic Fe,Ni (Fig. 7) is igneous and typical of metal quenched from melts (e.g., Smith and Goldstein 1977), and so are the highly variable Ni, and high P and S contents. Most of the metallic Fe,Ni is low in Ni, with approximately 7.5 Ni, 0.47 Co, 0.28 P, and 0.19 S (all in wt%) (Table 3). The low-Ni metal is rimmed in places at the boundaries with troilite by spottily zoned and more Ni-rich metallic Fe,Ni. The most Ni-rich phase (green in Fig. 7) has approximately 32.8 Ni, 0.49 Co, 0.29 P, and 0.36 S. The metallic Fe,Ni appearing brownish-green in Fig. 7 has approximately 20 Ni (Table 3; all in wt%), but there is considerable zoning from the low-Ni to the high-Ni areas. It should be noted that care was taken during the analysis of the metal to keep the electron beam of the EPMA away from the boundaries with troilite, so the S contents of the metal are real and are not caused by excitation of the S K$_\alpha$ X-ray line from overlap of the electron beam with troilite. It is also noteworthy that the metal in the Fe,Ni-FeS lithology does not contain Si and the troilite does not contain Ti, as does kamacite and troilite in EH and EL chondrites (e.g., Keil 1968) and in the LAR 04316 host (Table 3), and is generally the case for kamacite and troilite in aubrites (e.g., Watters and Prinz 1979; Casanova et al. 1993).

The mineralogy of the Fe,Ni-FeS lithology suggests that it might show evidence for the presence during its formation of ^{60}Fe, a short-lived radionuclide that decays to ^{60}Ni. Iron-60 has a half-life of approximately 2.6 Ma

Table 5. Trace element abundances (in ppm; by ICP-MS, or ICP-AES for Cr and Ni) in the enstatite-forsterite-diopside-glass vitrophyre lithology (subsample "18") from the LAR 04316 aubrite, and of the host LAR 04316 aubrite (subsample "40").

Elements	LAR 04316,18	LAR 04316,40	Elements	LAR 04316,18	LAR 04316,40
Li	2.50	0.789	La	0.244	0.178
Be	0.025	0.013	Ce	0.620	0.558
Sc	8.77	5.17	Pr	0.0956	0.0935
Ti	457	310	Nd	0.501	0.509
V	20.0	9.53	Sm	0.171	0.176
Cr	1323	624	Eu	0.0638	0.0345
Mn	2238	2195	Gd	0.231	0.252
Co	16.56	15.14	Tb	0.0431	0.046
Ni	346	369	Dy	0.297	0.309
Cu	4.48	11.97	Ho	0.0666	0.0688
Zn	4.19	4.74	Er	0.197	0.200
Ga	0.20	0.11	Yb	0.196	0.179
Rb	2.55	1.37	Lu	0.0298	0.0260
Sr	8.49	4.56	Hf	0.119	0.063
Y	1.73	1.64	Ta	0.013	0.012
Zr	4.09	2.17	W	0.006	0.028
Nb	0.13	0.13	Pb	0.044	0.022
Mo	< 0.02	< 0.02	Th	0.0324	0.0111
Ba	2.63	1.24	U	0.007	0.004

Fig. 7. Combined elemental map obtained in the EPMA in Fe (red), Ni (green), and S (blue) K_α X-rays of a portion of the Fe,Ni-FeS lithology LAR 04316,3, showing the quench texture of the metallic Fe,Ni dendritic/cellular structures with arm/cell spacings of approximately 30 μm, embedded in troilite. Ni-poor metal is red, Ni-rich metal is green; zoned metal with intermediate Ni contents is brownish-green; troilite is blue. Points marked 1 and 2 appear to be SiO_2, and point marked 3 appears to be a sodium-phosphorus-oxygen compound of unknown precise composition.

Fig. 6. Rare earth element (REE) abundances obtained by ICP-MS techniques and normalized to CI abundances (Evensen et al. 1978). A) The enstatite-forsterite-diopside-glass vitrophyre lithology (subsample "18") from the LAR 04316 aubrite, compared with the enstatite chondrites Indarch (EH4) and Hvittis (EL6) (J.-A. Barrat, unpublished data). B) The bulk host aubrite (subsample "40"), compared with aubrites (Wolf et al. 1983).

Fig. 8. Dendrite or cell size of metallic Fe,Ni dendrites plotted against globule diameter for rapidly cooled Fe,Ni-FeS globules that formed by impact melting of chondritic material (abbreviations are for chondrite names) and lunar spherules. Cooling rates during solidification, estimated from dendrite or cell sizes, are shown on the right ordinate. Three straight lines give cooling rates for metallic spheres cooling by radiation (top line), by conduction in the top layer of cold silica (middle), and in cold metal (bottom) (after Blau and Goldstein 1975; reprinted from Scott 1982, with permission from Elsevier). The approximately 30 μm arm/cell spacings for the Fe,Ni-FeS lithology LAR 04316,3 and the Fe,Ni-FeS inclusions in the vitrophyre suggest a quench rate of approximately 25–30 °C s^{-1} for the assemblages. The location of the point for the approximately 20 mm-sized Fe,Ni-FeS/vitrophyre clast between the middle and lower dashed lines calculated for cooling by conduction in cold silica and cold metal is consistent with the clast having quenched as a freely floating pyroclast, rather than as a fragment of a lava flow or dike conduit.

(Rugel et al. 2009) and, thus, has the potential to provide information about the formation time of the metal-sulfide lithology. Troilite typically strongly excludes Ni when it
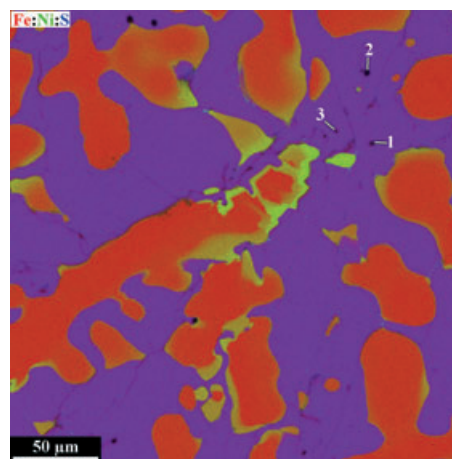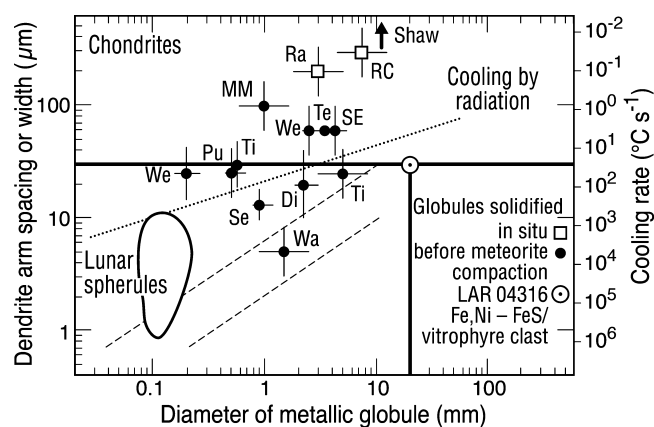
forms and, thus, tends to have a high Fe/Ni ratio. Unfortunately, the Fe/Ni ratio in the troilite is only approximately 130, which would give a maximum excess on ^{60}Ni of approximately 0.25‰, assuming an initial $^{60}Fe/^{56}Fe$ ratio of 5×10^{-7}. This is an order of magnitude too small to be resolved by ion microprobe techniques.

The Fe,Ni-FeS lithology contains a rather large inclusion approximately 600 μm in largest dimension (Figs. 2 and 9) that consists of very homogeneous alabandite, but its rim toward the troilite of the Fe,Ni-FeS lithology is much higher in iron (Table 3) and plots in the keilite field of the ternary diagram Fe-Mg-Mn + Ca + Cr (Fig. 5).

Mineralogy, Petrology, Bulk Chemical, and Oxygen Isotopic Compositions of the Enstatite-Forsterite-Diopside-Glass Vitrophyre

The average oxygen isotope composition of the vitrophyre LAR 04316,47, $\delta^{18}O = 4.61$‰, $\delta^{17}O = 2.28$‰, and $\Delta^{17}O = -0.14$‰, lies within the lowest range of EH chondrite compositions reported by Newton et al. (2000) and Miura et al. (2007) (Fig. 4). The uncertainties in $\delta^{18}O$, $\delta^{17}O$, and $\Delta^{17}O$ for LAR 04316,47, are 0.22‰, 0.16‰, and 0.06‰, respectively, smaller in $\delta^{18}O$ and $\delta^{17}O$ than those of the aubrite host but larger than those measured for USNM 107144. The dispersion in $\Delta^{17}O$ values of the vitrophyre is due to a single analysis with $\delta^{18}O = 4.71$ ‰, $\delta^{17}O = 2.44$‰, and $\Delta^{17}O = -0.04$‰. Removing this analysis gives average values of $\delta^{18}O = 4.58$ (± 0.24)‰, $\delta^{17}O = 2.24$ (± 0.15)‰, and $\Delta^{17}O = -0.17$ (± 0.03)‰. We suggest that the outlying analysis resulted from inadvertent inclusion of a large grain of enstatite in the analyzed vitrophyre sample (Fig. 4).

The $\delta^{18}O$ values of aubrite host and vitrophyre overlap, but their $\Delta^{17}O$ values −0.01 (± 0.03)‰ and −0.17‰ (±0.03)‰, differ significantly (see above). Most aubrite oxygen isotope analyses reported in the literature lie close to the terrestrial fraction line with average $\Delta^{17}O = 0.0 \pm 0.04$‰ (Clayton and Mayeda 1996; Newton et al. 2000; Miura et al. 2007). The heterogeneity in $\Delta^{17}O$ measured in this study is unusual but has been observed in several aubrites, notably in Cumberland Falls, where $\Delta^{17}O$ values range from −0.06 to +0.34‰ (Miura et al. 2007). Newton et al. (2000) reported $\Delta^{17}O = +0.531 \pm 0.05$‰ for Cumberland Falls (Fig. 4). The heterogeneity in $\Delta^{17}O$ for Cumberland Falls most likely arises from the presence of L or LL chondrite inclusions (Newton et al. 2000; Miura et al. 2007). We suggest that the heterogeneity in $\Delta^{17}O$ of the LAR 04316,47 vitrophyre is the result of its mineralogical and chemical heterogeneity and the existence of inclusions such as the enstatite inclusion (see below).

Polished thin section LAR 04316,4 is dominated by the vitrophyre lithology, but also has some of the aubrite
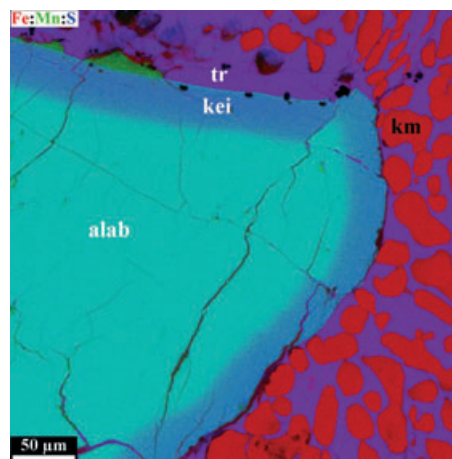

Fig. 9. Combined elemental map obtained in the EPMA in Fe (red), Mn (green), and S (blue) K_α X-rays of the alabandite-keilite inclusion (center) in the LAR 04316,3 Fe,Ni-FeS lithology (right). The alabandite inclusion (alab) is light greenish-blue, its keilite (kei) border is dark blue, troilite (tr) is purple, and the low-Ni metallic Fe,Ni (km) dendrites are red.

host regolith breccia material attached to it. The vitrophyre consists of abundant enstatite and forsterite. Both enstatite ($Fs_{2.37}$) and forsterite ($Fa_{1.88}$) are low in FeO, but not as low as enstatite ($Fs_{0.07}$) in the host aubrite (Table 2). Due to its small size, we were able to reliably analyze only one grain of diopside of approximately $Wo_{42.6}En_{57.4}Fs_{<0.1}$, which is very similar in composition to this mineral in the host aubrite (approximately $Wo_{42.9}En_{57.0}Fs_{<0.1}$; Table 2), including being very low in FeO. Some of the enstatites are lath-shaped in texture and up to approximately 1 mm in longest dimension, while others poikilitically enclose relatively coarse-grained, blocky forsterite crystals up to approximately 100 μm in size (Fig. 10). The vitrophyre has a typical quench texture, suggesting very fast cooling, as is indicated by the occurrence in the mesostasis between larger forsterite and enstatite crystals of enstatite crystals with hopper textures (Fig. 10). These crystals frequently have mantles of diopside, and skeletal diopside laths are also abundant. The enstatite hopper-textured crystals and the diopside laths are embedded in an interstitial silica-rich material which we refer to as glass (Fig. 10; Table 2), although due to the small sizes of these areas, it is impossible to judge in the optical microscope whether or not this material is actually isotropic. While we have analyzed many of the interstitial glass areas, the analyses in Table 2 are for the four largest areas found in the section and are least contaminated by the electron beam of the EPMA overlapping enstatite-diopside quench crystals during analysis, as is indicated by the highest SiO_2 contents measured (average 76.2 wt%). In addition, this glass is also rich in Al_2O_3 (8.3), CaO (5.7), Na_2O (2.14), and K_2O
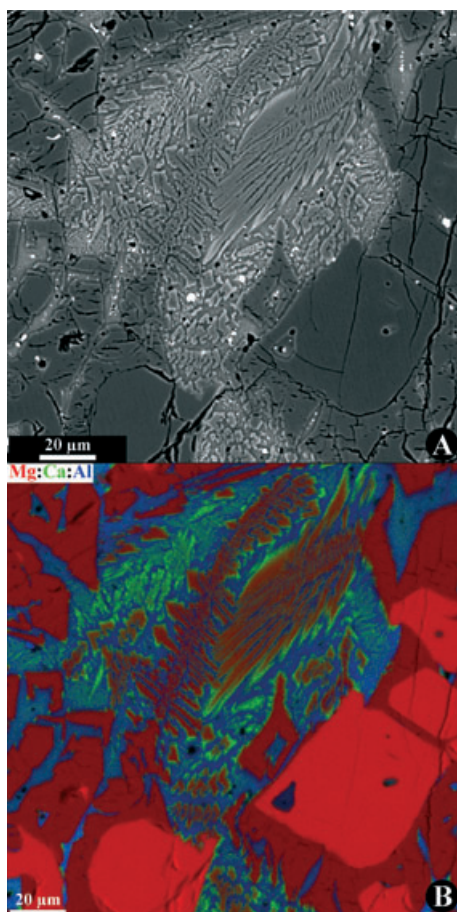
Fig. 10. Backscattered electron (BSE) image (A) and combined elemental map (B) obtained in the EPMA in Mg (red), Ca (green) and Al (blue) K$_\alpha$ X-rays of a portion of the LAR 04316,4 vitrophyre, illustrating the vitrophyric quench texture of the clast. A) The white phase is mostly troilite, with some metallic Fe,Ni. B) Blocky forsterite crystals are red and usually poikilitically enclosed in enstatite (brown). The fine-grained interstitial mesostasis consists of enstatite crystals with hopper textures (brown), zoned diopside laths (green) which frequently mantle the hopper-textured enstatite, and a SiO$_2$-Al$_2$O$_3$-CaO-Na$_2$O-K$_2$O-rich and TiO$_2$-FeO-MnO-MgO-bearing glass (blue).
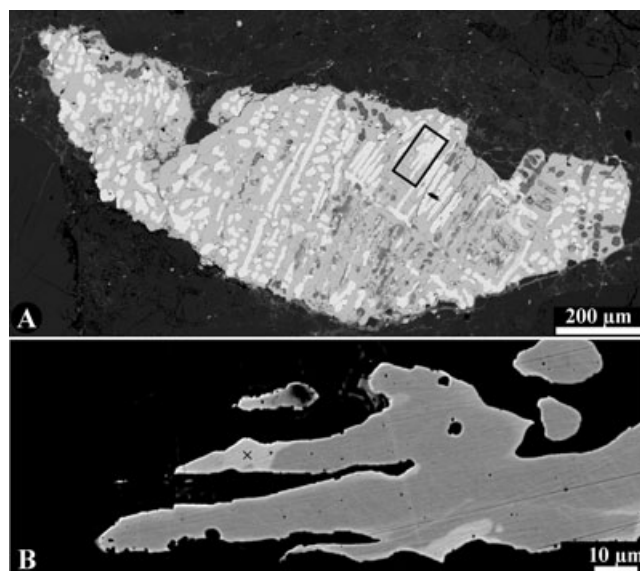

Fig. 11. Backscattered electron images obtained in the EPMA of (A) a quench-textured troilite (gray)-metallic Fe,Ni (white) inclusion approximately 1500 μm in longest dimension. It occurs on the boundary of the vitrophyre and the brecciated aubrite host portion and actually is partly included into the vitrophyre. It resembles in texture and composition the approximately 10 mm-sized LAR 04316,3 Fe,Ni-FeS lithology (compare with Figs. 2, 3 and 7). The metallic Fe,Ni in this inclusion has the same spotty zoning in Ni content and the same dendritic/cellular structure as in the large LAR 04316,3 Fe,Ni-FeS lithology, and the arm/cell spacings are similarly approximately 25–30 μm, indicating very fast cooling of approximately 25–30 °C s^{-1}. Small dark objects are hydrous iron oxides formed by the terrestrial weathering of metallic Fe,Ni (EPMA only shows low Fe). B): BSE magnified image of the outlined rectangular area in (A), showing that the metallic Fe,Ni is spottily zoned in Ni. The white areas are high and the gray low in Ni; the x indicates the position of the analytical point of the Ni-rich metallic Fe,Ni listed in Table 6. The silicate background of the rock has purposely been kept dark to enhance the appearance of the Fe,Ni-FeS inclusion.

(0.36) and also contains TiO$_2$ (0.22), FeO (2.76), MnO (0.41), and S (0.19; all in wt%). Its CIPW wt% norm calculates to 43.52 quartz, 29.73 plagioclase, 2.13 orthoclase, 13.00 diopside, 10.81 hypersthene, 0.42 ilmenite, and 0.40 pyrite. This glass resembles somewhat in composition some of the silicate glasses analyzed in aubrite basalt vitrophyres by Fogel (2005), including its minor S content of 0.19%, which he attributes to the high degree of reduction of the assemblage, although the glass in this vitrophyre is not identical to any of the glasses analyzed by Fogel (2005) (see Discussion).

The vitrophyre is in contact with, and partially engulfs, an inclusion approximately 1500 μm in size consisting of an Fe,Ni-FeS assemblage (Fig. 11) which closely resembles in texture and composition the large Fe,Ni-FeS lithology LAR 04316,3. It has the same dendritic/cellular structure and arm/cell spacings of approximately 25–30 μm, indicating that it also cooled at approximately 25–30 °C s^{-1} (compare Fig. 11 with Figs. 2, 3 and 7). The metallic Fe,Ni in this inclusion is mostly Ni-poor, but in places it has, on its edges, a Ni-rich phase (Fig. 11B) very similar in occurrence and composition (Table 6) to the Ni-rich phases in the large LAR 04316,3 Fe,Ni-FeS lithology (Table 3). This inclusion occurs on the boundary of the vitrophyre and the brecciated aubrite host portion and actually is partly included within the vitrophyre, suggesting that this and the large Fe,Ni-FeS quench lithology LAR 04316,3 and the vitrophyre are cogenetic and were molten and cooled simultaneously.

Table 6. Average electron microprobe analyses of Ni-rich (Ni-r) and Ni-poor (Ni-p) metallic Fe,Ni in the Fe,Ni-FeS inclusion (Fe-I) (Fig. 11) attached to and partly within the enstatite-plagioclase-diopside-glass vitrophyre lithology, and of sulfides and metallic Fe,Ni in the troilite-keilite-metallic Fe,Ni globule (G1) shown in Fig. 13A and of troilite, Ni-poor (Ni-p), and Ni-rich (Ni-r) metallic Fe,Ni in the troilite-metallic Fe,Ni globule (G2) shown in Fig. 13B from the enstatite inclusion within the enstatite-plagioclase-diopside-glass vitrophyre lithology LAR 04316,4 (in wt%). Mineral abbreviations as in Table 3.

	Fe-I	Fe-I	G1	G1	G1	G2	G2	G2
	Ni-r	Ni-p	Tr	K	Fe	Tr	Ni-p	Ni-r
N	1	3	12	12	10	5	4	4
Fe	66.4	91.9	61.7	40.2	89.0	65.0	90.5	78.0
Mn	n.d.	n.d.	1.31	21.6	n.d.	0.07	n.d.	n.d.
Cr	n.d.	n.d.	1.78	1.14	n.d.	0.53	n.d.	n.d.
Ti	n.d.	n.d.	0.09	0.02	n.d.	b.d.	n.d.	n.d.
Mg	n.d.	n.d.	0.05	0.20	n.d.	0.08	n.d.	n.d.
Ca	n.d.	n.d.	b.d.	0.38	n.d.	b.d.	n.d.	n.d.
S	0.33	0.16	37.0	36.8	0.45	36.5	0.28	0.61
Ni	31.0	7.46	n.d.	n.d.	8.32	n.d.	6.98	18.1
Co	0.52	0.47	n.d.	n.d.	0.55	n.d.	0.49	0.53
Si	b.d.	b.d.	n.d.	n.d.	0.04	n.d.	0.04	0.06
P	0.47	0.28	n.d.	n.d.	0.34	n.d.	0.44	0.41
Total	98.72	100.27	101.93	100.34	98.70	102.18	98.73	97.71

Notes: N = number of analyses; b.d. = below detection; n.d. = not determined.

The vitrophyre also contains an inclusion (herein referred to as the enstatite inclusion), about 2.4 mm in largest dimension, that consists largely of enstatite ($Fs_{0.33}Wo_{0.62}$; Table 2), with traces of forsterite too small for reliable quantitative EPMA, and globules of metallic Fe,Ni, troilite, and keilite (Fig. 12A). This inclusion is clearly embedded in the vitrophyre, as indicated in Fig. 12A by the typical quenched vitrophyre assemblage of enstatite-forsterite-diopside-glass that surrounds the enstatite inclusion. It is cut by a vein with contact to the main vitrophyre (Figs. 12A and 12B) that is composed of skeletal diopside quench crystals and an SiO_2-rich glass, similar in mineralogy and composition to the diopside-glass interstitial material in the surrounding main mass of the vitrophyre. In places, the vein also contains small enstatite ($Fs_{1.70}Wo_{0.30}$) and forsterite ($Fa_{0.86}$) crystals (Table 2) and some sulfide-metal droplets (Fig. 12B). Due to the small sizes of the SiO_2-rich mesostasis areas, we were unable to verify in the optical microscope if this material is actually isotropic. BSE images obtained in the EPMA at high magnification of 9500× indicate that the diopside crystals are at most 10–20 μm long and approximately 1.5 μm wide, and the interstitial glass areas are approximately of the same sizes. The small sizes prevented accurate quantitative EPMA of the crystals and glass, but semiquantitative EDS analyses confirm that the crystals are pyroxene with major Mg and Ca and minor Al, presumably diopside, and the glass is rich in SiO_2 and contains major Al and appreciable Mg and Ca, not unlike the glass in the vitrophyre (Table 2). However, we have analyzed with

the EPMA seven areas in the vein using a broad electron beam of 5 μm to determine its bulk composition (Table 2). Analyses of these seven different areas do not vary much, presumably due to the small sizes of the diopside crystals and glass areas, and are high in SiO_2 (67.3), Al_2O_3 (9.2), MgO (8.4), and CaO (9.5) and also contain minor FeO (2.29), MnO (0.95), Na_2O (0.41), K_2O (0.39), TiO_2 (0.35), and S (0.19) (all in wt%).

This inclusion also contains several metallic Fe,Ni-sulfide spherical (i.e., once molten) globules (Fig. 12A). One of these is about 100 μm in diameter and consists of metallic Fe,Ni dendrites with arm/cell spacings of approximately 20 μm, embedded in troilite (Fig. 13B), indicating very fast cooling of approximately 80 °C s^{-1} (Fig. 8). The metallic Fe,Ni is mostly Ni-poor, with 6.98 Ni, 0.28 S, 0.49 Co, 0.04 Si, and 0.44 P, but there are also some Ni-rich areas on the borders of the Ni-poor phase (Fig. 13B), with 18.1 Ni, 0.61 S, 0.53 Co, 0.06 Si, and 0.41 P. The troilite contains 0.07 Mn, 0.53 Cr, and 0.08 Mg, but Ti is below the detection limits (all in wt%; Table 6). The other globule is approximately 210 μm in the longest dimension and also consists of metallic Fe,Ni dendrites, but these are embedded into a blocky intergrowth of troilite and keilite; note that this globule is surrounded by numerous smaller ones of the same type and composition (Fig. 13A). The metallic Fe,Ni in this globule varies somewhat in Ni (7.74–10.12, average 8.32%), and also contains 0.45 S, 0.55 Co, 0.04 Si, and 0.34 P. The troilite contains 1.31 Mn, 1.78 Cr, 0.09 Ti, and 0.05 Mg. Keilite is the most Fe-rich (40.2) and Mg-poor (0.20) in this meteorite, but also contains 21.6 Mn,
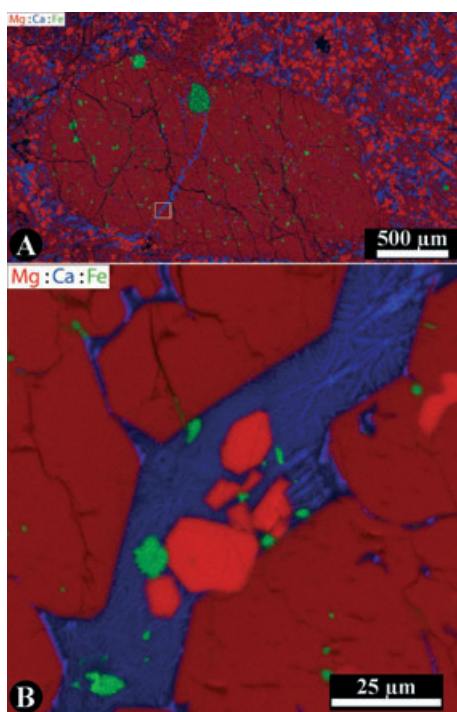
Fig. 12. Combined elemental maps obtained in the EPMA in Mg (red), Ca (blue), and Fe (green) K_α X-rays of the enstatite inclusion within the LAR 04316,4 vitrophyre lithology (A) which consists largely of enstatite (brown), with traces of forsterite (red). Metallic Fe,Ni (green) occurs with sulfides (grayish-brown). The inclusion is surrounded by the vitrophyre lithology which consists of skeletal enstatite (brown) and forsterite (red), embedded in a diopside and SiO_2-rich glass matrix (blue). B) The vein outlined in (A) by the white rectangle originates in the vitrophyre and consists mostly of extremely fine-grained, skeletal diopside quench crystals, and SiO_2-rich glass (blue). The surrounding crystals are enstatite (brown), occasionally including forsterite (red), and the vein contains a few small forsterite crystals (red) and sulfide-metallic Fe,Ni grains (green).

Fig. 13. Combined elemental maps obtained in the EPMA in Fe (red), Mn (green), and S (blue) K_α X-rays of (A) the metallic Fe,Ni (red)-troilite (purple)-keilite (greenish-blue) globule shown in the upper center of Fig. 12A, and (B), of the metallic Fe,Ni (red)-troilite (purple) globule shown in the upper left of Fig. 12A, from the enstatite inclusion within the LAR 04316,4 vitrophyre lithology. A) Throughout the surrounding enstatite (black) are scattered small Fe,Ni-troilite-keilite inclusions. The dendritic/cellular structure is similar to that of the large LAR 04316,3 Fe,Ni-FeS lithology, and the arm/cell spacings are similarly approximately 30 μm, indicating very fast cooling of approximately 25–30 °C s^{-1}. B) The brownish-reddish areas associated with the red Fe,Ni are more Ni-rich metallic Fe,Ni, (Table 6), and the several green spots are probably alabandite or keilite. The dendritic/cellular structure of this globule is also similar to that of the large LAR 04316,3 Fe,Ni-FeS lithology, and the arm/cell spacings are similarly approximately 20 μm, indicating very fast cooling of approximately 80 °C s^{-1}. The backgrounds in both images were purposely kept black to enhance the appearance of the objects.

1.14 Cr, 0.02 Ti, and 0.38 Ca (all in wt%; Table 6). The arm/cell spacings of the metallic Fe,Ni of approximately 30 μm also suggest cooling at a rate of approximately 30 °C s^{-1}. Thus, these globules provide additional evidence that the vitrophyre and its enclosed enstatite inclusion cooled as rapidly as the large Fe,Ni-FeS lithology LAR 04316,3, and that they all were molten and cooled simultaneously.

We have determined the major, minor, and trace element compositions of the vitrophyre, and compared the major and minor element compositions with that of average aubrites (Table 4). In keeping with the mineralogy and mineral chemistry of the vitrophyre, its composition is more evolved and differentiated than average aubrite, as many oxides that tend to be enriched in partial melts are higher in the vitrophyre than in average aubrite. S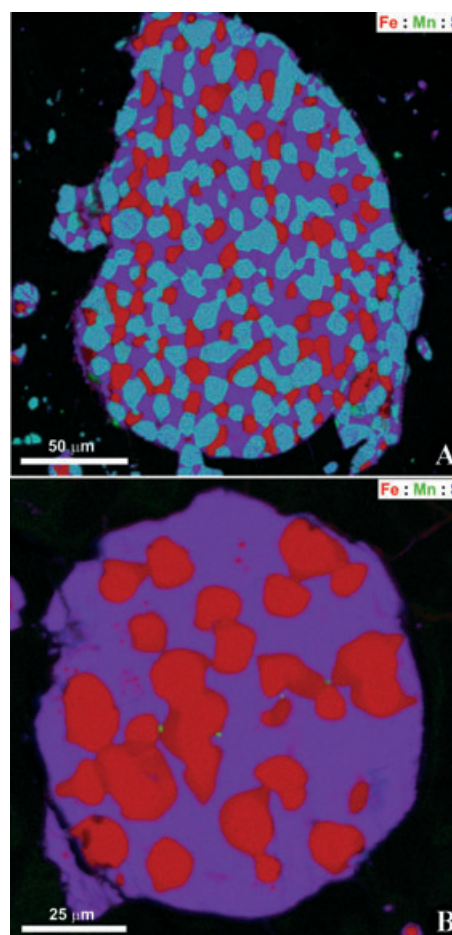pecifically, vitrophyre Al_2O_3 is 1.79 versus 0.8 in average aubrite; CaO is 1.70 versus 0.94; Na_2O is 0.80 versus 0.41; K_2O is 0.10 versus 0.02; FeO is 3.48 versus 0.05; MnO is 0.33 versus 0.04; TiO_2 is 0.08 versus 0.05; and Cr_2O_3 is 0.19 versus 0.03; note that MgO in the vitrophyre is 35.4 versus 38.1 in average aubrite (Table 4; all in wt%).

We also determined the REE abundances of the vitrophyre lithology (Fig. 6A). In spite of the seemingly differentiated nature of this lithology, the REE abundances and the shape of the REE pattern are nearly chondritic (e.g., $La_n/Sm_n = 0.90$; $Gd_n/Lu_n = 0.97$), with no significant Eu anomaly ($Eu/Eu* = 0.98$). The abundances and the pattern of the vitrophyre are quite different from those of aubrites, however, most of which have lower REE abundances and strong negative Eu anomalies (Figs. 6A and 6B).

DISCUSSION

Below, we discuss the evidence we have accumulated in regard to the origin of the Fe,Ni-FeS and vitrophyre lithologies as a pyroclast formed during explosive volcanism on the aubrite parent body. We also summarize our evidence against an impact origin of the clast.

Comparison of the Vitrophyre LAR 04316,4 to the Aubrite Basalt Vitrophyres Described by Fogel (2005)

McCoy and Gale (2006) drew attention to the similarities in composition and mineralogy between the vitrophyre LAR 04316,4 and the three aubrite vitrophyre basalt clasts (AVBs) described by Fogel (2005) from the Parsa enstatite chondrite and the Khor Temiki and Lewis Cliff (LEW) 87007 aubrites. Fogel (2005) interpreted these clasts as remnants of the pyroclastic volcanism on the aubrite parent body postulated by Wilson and Keil (1991) and of the elusive enstatite-plagioclase basalts. (Note, however, that Nehru et al. [1984] and Keil [2007] interpreted the Parsa clast, and Keil [2007] interpreted the Khor Temiki clast as impact-melt clasts of enstatite chondrite parentage.)

Whereas most pyroclasts may have escaped the aubrite parent body during early pyroclastic volcanism, as postulated by Wilson and Keil (1991), McCoy and Gale (2006) concluded that the LAR 04316,4 vitrophyre may be a pyroclast that was retained on the aubrite parent body by virtue of its relatively large size. As shown by Wilson et al. (2010), 20 mm-sized clasts like the LAR 04316,4 Fe,Ni-FeS—vitrophyre clast can be retained under certain conditions on the asteroidal-sized aubrite parent body (see below).

Whereas there are some similarities in the properties of the ABVs of Fogel (2005) and the vitrophyre lithology LAR 04316,4, in detail the latter is quite different from the former. For example, the vitrophyre LAR 04316,4 is actually part of a single, 20 mm-sized clast consisting of two immiscible liquids, represented by the Fe,Ni-FeS and the silicate vitrophyre lithologies. In addition, the vitrophyre contains smaller metallic Fe,Ni-FeS inclusions

which is not the case for the ABVs. Since we have determined the cooling rates of the Fe,Ni-FeS lithology and the Fe,Ni-FeS inclusions in the vitrophyre, the cooling rate of a vitrophyre lithology can also be estimated (see below). While Fogel (2005) argued for cooling rates of his ABVs as "not very rapid," based on the silicate textures and crystal sizes, the presence of the associated Fe,Ni-FeS lithology in the pyroclast described herein allows us to put the first quantitative constraints on the cooling rate of our vitrophyre. Furthermore, the vitrophyre LAR 04316,4 is larger than the ABVs described by Fogel (2005), the largest of which is < 7.8 mm in largest dimension. There are also some important differences in mineralogy and composition: The Khor Temiki, Parsa and LEW 87007 clasts have approximately 44, 24, and 10 clear, isotropic glass, approximately 11, 0.4, and 0.7 forsterite, approximately 44, 74, and 82 enstatite, and no diopside except for approximately 6 in L871, whereas the normative mineralogy calculated from the bulk composition of the vitrophyre LAR 04316,4 suggests approximately 8 plagioclase (presumably in the glass), 6 diopside, 70 enstatite, and 17 forsterite (all in wt%). Qualitative estimates of the phase abundances in Fig. 10 are in agreement with the calculated norm and clearly show the high forsterite and low glass contents of the vitrophyre. The mesostasis of the LAR 04316,4 vitrophyre is microcrystalline and nearly opaque in thin section in transmitted light due to its fine grain size, whereas the mesostases in the ABVs consist of clear glass. Specifically, the LAR 04316,4 mesostasis consists of quench crystals of enstatite with hopper textures, often mantled by diopside, and of skeletal quench diopside laths up to several tens of μm in the longest dimension (Fig. 10), all embedded in a SiO_2-rich glass. In contrast to Fogel's (2005) ABVs, the glass areas in the LAR 04316,4 vitrophyre are too small to judge with confidence in the optical microscope whether or not the material is actually isotropic.

There are also considerable differences in bulk compositions between the LAR 04316,4 vitrophyre and the ABVs in the Khor Temiki enstatite chondrite (KT1) and the Parsa aubrite (PA1) (Table 7). Specifically, SiO_2, Al_2O_3, Na_2O, and K_2O are lower and FeO, MnO, MgO, and CaO are higher in the LAR 04316,4 vitrophyre. The LAR 04316,4 vitrophyre bulk composition superficially resembles most closely the bulk composition of clast L871 in the Lewis Cliff LEW 87007 aubrite, although the FeO, MnO, and CaO are higher in the former. While there are also similarities in the compositions of the glass in the LAR 04316,4 vitrophyre and the three ABVs, there is no close match for any of them (Table 7). Specifically, SiO_2, FeO, MnO, and CaO are higher, and Al_2O_3, Na_2O, and K_2O are lower in the vitrophyre.

Table 7. Comparison of the bulk and glass mesostasis compositions of the enstatite-forsterite-diopside-glass vitrophyre lithology in LAR 04316 (subsample "18") with the bulk silicate portions and the glass of the aubrite basalt vitrophyre clasts KT1, PA1, and L871 of Fogel (2005) (in wt%). Note that the last three contain less than 1% metal and sulfides.

Oxides	LAR 04316,18 bulk	KT1 bulk	PA1 bulk	L871 bulk	LAR 04316,4 glass	KT1 glass	PA1 glass	L871 glass
SiO_2	56.1[a]	62.58	61.90	60.61	76.2	69.78	67.79	74.13
TiO_2	0.08	0.11	0.04	0.04	0.22	0.24	0.16	0.24
Al_2O_3	1.79	4.82	3.63	1.69	8.3	10.75	14.41	16.61
Cr_2O_3	0.19	n.d.	n.d.		n.d.	b.d.	b.d.	b.d.
FeO	3.48	0.22	0.15	0.55	2.76	0.16	0.26	0.15
MnO	0.33	0.04	0.04	0.18	0.41	b.d.	b.d.	b.d.
MgO	35.40	26.32	30.67	34.88	4.9	5.52	3.96	0.26
CaO	1.70	1.48	1.28	1.15	5.7	3.15	4.56	0.20
Na_2O	0.80	2.99	1.47	0.77	2.14	6.67	5.84	7.76
K_2O	0.10	1.07	0.80	0.10	0.36	2.42	0.80	0.98
P_2O_5	0.01	n.d.	n.d.	n.d.	n.d.	n.d.	n.d.	n.d.
S	n.d.	0.37	0.63	0.01	0.19	0.84	2.56	0.08
Total	99.98	99.70	100.44	99.98	101.18	99.53	100.34	100.41

Notes: n.d. = not determined; b.d. = below detection.
[a]Determined by difference to 100.

A Caveat: Origin of the Clast by Impact Melting?

We argue for an origin of the LAR 04316 Fe,Ni-FeS–vitrophyre clast as a pyroclast of internally derived, relatively high-degree partial melts, formed during pyroclastic volcanism on the aubrite parent body. Whereas we cannot totally rule out an origin of the clast by impact melting, several lines of evidence argue against such an origin.

Clearly, the Fe,Ni-FeS–vitrophyre clast does not represent melting of the bulk aubrite, being significantly enriched in feldspathic, metal (both modally and as reflected in Co and Ni enrichments), and sulfide components compared with the aubritic host, as well as differing in oxygen isotopic composition. Thus, any impact melting scenario would require melting of an enstatite chondrite-like target or impactor. If the Fe,Ni-FeS–vitrophyre clast originated by impact melting on an enstatite chondrite-like parent body, it would then have to be ejected from the parent asteroid and be transported to the aubrite parent body where it would have to be buried in the dynamic surface regolith. In this case, the delicate Fe,Ni-FeS–vitrophyre clast is not likely to have survived impact melting on one asteroid (the enstatite chondrite-like parent object) and transport to and burial in the dynamic surface regolith of another asteroid (the aubrite parent body). Alternatively, an enstatite chondrite-like impactor could have melted when it collided with the aubrite parent body. Indeed, one might argue that the relatively unfractionated, REE pattern of the vitrophyre (Fig. 6) suggests formation by impact melting. However, Fogel (2005) has argued that the rather flat and chondritic REE pattern of a vitrophyre does not necessarily suggest an origin by impact melting. He points out that the REE in enstatite chondrites are nearly totally in oldhamite (e.g., Floss and Crozaz 1993; Lodders 1996). Since oldhamite is very soluble in enstatite chondrite melts (Fogel et al. 1996; McCoy et al. 1999), the REE will remain in the partial melt and, hence, the vitrophyre crystallizing from this melt will have a rather flat and unfractionated, chondritic REE pattern.

Alternatively, if the aubrite parent body had retained a thin unmelted exterior veneer of its enstatite chondrite-like parent lithology of the aubrites, impact melting of this veneer could have occurred on the aubrite parent body and produced this clast. However, then the 21 known brecciated aubrites should commonly contain enstatite chondrite-like clasts, which is not the case (Keil 2010).

An additional line of evidence against an impact origin of the ABVs was offered by Fogel (2005) and also applies to the clast in LAR 04316. Although the bulk silicate composition of the composite clast is nearly chondritic, the metal:troilite ratio is clearly not similar to enstatite chondrites (Keil 1968). In the LAR 04316 clast, the metal:troilite ratio is approximately 1, whereas bulk enstatite chondrites have metal:troilite ranging from approximately 2 to 4. As noted by Fogel (2005), this enrichment in troilite is consistent with melting along the Fe,Ni-FeS cotectic, but inconsistent with impact melting. Since impacts cannot produce partial but only total melts (Keil et al. 1997), the vitrophyre is not likely to be an impact melt of an enstatite chondrite-like parent lithology. Indeed, one might argue that impact melting might produce an overabundance of metal relative to

troilite owing to S volatilization during the impact, quite opposite to what we observe in this clast.

Finally, it is worth noting that some of the features in the LAR 04316 clast are similar to those observed by Fogel (2005) in the L871 clast and attributed by him to formation at a higher fO_2. The higher FeO concentration of mafic silicates in the LAR 04316 clast compared with the aubrite host (Table 2) or enstatite chondrites, the near absence of Si in its metal (Tables 3 and 6) or Ti (Table 3) in its troilite, and the abundance of olivine are all unlike enstatite chondrites. This suggests both that the clast did not form through simple impact melting of an enstatite chondrite-like protolith, and that oxidation occurred during melting or crystallization. The features of the LAR 04316 clast are consistent with formation at a higher fO_2 where oxidation of Fe metal to FeO stabilizes forsterite in the crystallizing melt at the expense of enstatite. Although the source of oxygen for such an event is uncertain, it need not be an abundant source. The mineral compositions in the LAR 04316 clast are similar to those observed in winonaites, which formed at an fO_2 of approximately IW-3 (Benedix et al. 2005). Although this is approximately 2 log units above the ambient fO_2 of aubrites, a gas driving pyroclastic volcanism containing as little as 1% CO_2 could buffer the melt at this higher oxygen fugacity. We suggest the possibility that decomposition of sinoite in the enstatite chondrite like precursor might be capable of producing the necessary oxygen.

Simultaneous Origin of the Fe,Ni-FeS and Vitrophyre Lithologies by Quench of a Composite Metal-Sulfide/ Silicate Immiscible Melt Droplet, and Cooling as a Freely Floating Pyroclast

McCoy and Gale (2006) pointed out that the Fe, Ni-FeS and vitrophyre lithologies are joined at an igneous, common border, as is readily apparent from Fig. 1. This suggests that both lithologies were in physical contact while molten and while being quenched from high temperature. Also, the occurrence within the vitrophyre of smaller Fe,Ni-FeS inclusions of essentially identical compositions and textures, including dendrite/cell distances, to the 10 mm-sized Fe,Ni-FeS lithology (compare Figs. 11, 13A and 13B, with Figs. 2, 3 and 7) is additional evidence for their simultaneous origin. These observations also imply that the vitrophyre lithology cooled at approximately the same rate as the Fe,Ni-FeS lithology and clasts. Based on the approximately 30 μm spacing between the Fe,Ni dendrite arms in the lithologies and the inclusions, Fig. 8 yields an estimated cooling rate of approximately 25–30 °C s^{-1}. Thus, the vitrophyre lithology was similarly quenched at approximately that rate, which is totally consistent with its

quench texture (Fig. 10). It should also be noted that the occurrence of keilite as a reaction rim on the alabandite inclusion in the Fe,Ni-FeS lithology (Fig. 9), and as blocky grains in the metallic Fe,Ni-troilite-keilite globule in the enstatite inclusion within the vitrophyre (Fig. 13A), testify to the fast cooling (quench) of the assemblage: Skinner and Luce (1971) showed experimentally that whereas at high temperature, FeS is soluble in MnS, forming keilite, this high iron solid solution phase would exsolve FeS during slow cooling and is only metastable if quenched. Figure 5 shows that keilite in the inclusion in the Fe,Ni-FeS lithology plots approximately on the 660 °C ternary solvus line, and keilite in the enstatite inclusion within the vitrophyre on the 770 °C ternary solvus line experimentally determined by Skinner and Luce (1971) for the system FeS-MgS-MnS. This observation suggests that the minimum formation temperature for keilite from which it was quenched was approximately 660 °C for the former and approximately 770 °C for the latter. A quench origin of keilite is also confirmed by its occurrence in other quenched and rapidly cooled melts, in this case in enstatite chondrite impact-melt rocks and breccias (Keil 2007).

In Fig. 8 are also plotted curves that give the cooling rates for metallic spheres cooling by radiation (top line), by conduction in the top layer of cold silica (middle), and in cold metal (bottom) (Blau and Goldstein 1975; Scott 1982). The position of the point for the 20 mm-sized Fe,Ni-FeS–vitrophyre clast between the middle and lower dashed lines calculated for cooling by conduction in cold silica and cold metal, respectively, is consistent with the clast having cooled and been quenched as a freely floating pyroclast in the vacuum of space of the aubrite parent body. This also suggests that the clast is not, for example, an impact-comminuted piece of a dike or deeper igneous layer of the parent body, which presumably would have cooled at a much lower rate.

The modeling of Wilson and Keil (1991) dealt with silicate melts and showed that pyroclastic volcanism on a body like the aubrite parent body can produce silicate partial melt pyroclasts. Furthermore, the modeling of Keil and Wilson (1993) showed that Fe,Ni-FeS partial melts can also be accelerated to erupt as pyroclasts during partial melting of asteroids. In addition, Wilson et al. (2010) argued that there must commonly have been simultaneous migration of Fe,Ni-FeS and silicate melts, as significant silicate partial melting was required before efficient Fe,Ni-FeS liquid migration began (e.g., Taylor 1992; McCoy et al. 1997a, 1997b). While buoyancy would suggest that Fe,Ni-FeS melt would move downward and silicate melt upward in an asteroidal setting, the presence of free gas and gas bubbles in Fe,Ni-FeS melt pockets could make them buoyant and carry them upward to the asteroid surface together with silicate melts (Keil and Wilson 1993). Thus, we suggest that it should not be very

surprising that rare batches of immiscible Fe,Ni-FeS–silicate vitrophyre melts formed occasionally and rose simultaneously to be disrupted into droplets by shear forces or gas bubble expansion as they approached the surface of the small asteroidal parent body in an episode of pyroclastic volcanism. As we show below, unless unrealistically high volatile contents are assumed for the melts, droplets approximately 20 mm in size are too large to escape the gravity of the parent body and, thus, must fallback on its surface and be embedded into the regolith.

Finally, the heterogeneity in the $\Delta^{17}O$ values for the LAR 04316,47 vitrophyre (Fig. 4) is consistent with the proposition that the clast formed by pyroclastic volcanism: While most of the achondritic meteorite groups define a specific oxygen isotope mass-fractionation line (e.g., Greenwood et al. 2005; Day et al. 2009), ureilites, acapulcoites, lodranites, and winonaites are heterogeneous in $\Delta^{17}O$ values. Most workers ascribe such heterogeneity to incomplete melting and mixing during magmatism on the respective parent bodies, resulting in a failure to homogenize and equilibrate oxygen isotopes before cooling to the solidus. In the case of aubrites, only a few examples of variation in $\Delta^{17}O$ are known but, of course, only a few examples of aubrites containing readily identifiable clasts are known, either. We speculate that pyroclastic volcanism, as proposed for the aubrite parent body, would be effective in prematurely terminating melting and differentiation by catastrophic expulsion before continued mixing had succeeded in homogenizing the parent body.

Parent Body Size, Magma Volatile Content, Volatile Composition, and Pyroclast Density and Size

In proposing that explosive volcanism might have ejected silicate mantle melts from the aubrite parent asteroid as pyroclasts, Wilson and Keil (1991) assumed that the sizes of these pyroclasts would be very small, probably in the range of a few tens to hundreds of μm. They based their assumption on the observation (Weitz et al. 1997) that this is the size distribution of the glass beads found in the lunar regolith and identified as being the products of pyroclastic volcanism early in lunar history (Sato 1979; Fogel and Rutherford 1995). This lunar pyroclast observation is consistent with the theoretical prediction (Wilson and Head 1981) that a size distribution of this kind is always expected when explosive eruptions occur on bodies without atmospheres, so that extreme expansion of small gas bubbles nucleating in the erupting magmas can occur. Wilson and Keil (1996) revised their earlier estimate and concluded that the pyroclast sizes may have ranged from approximately 30 μm to 4 mm. Wilson et al. (2010) again revisited the issue of the pyroclast size distributions to be expected on asteroids

and showed that the absence of an atmosphere is not the only important controlling factor; asteroid size and hence internal pressure are also important. Thus, when mantle melting begins in an asteroid with a diameter significantly greater than 100 km, volatiles incorporated into the asteroid at the time of its accretion can dissolve into the silicate melt. As this melt approaches the surface through veins and fractures (i.e., dikes) and the pressure decreases toward the external vacuum, volatiles exsolve again as gas bubbles. The energetics of the bubble nucleation process (Sparks 1978) ensure that these gas bubbles are small, approximately 20 μm in diameter, expanding by decompression to a few hundred μm by the time they become close-packed, causing magma disruption into pyroclasts with range of sizes like that predicted by Wilson and Head (1981).

However, the pressures inside smaller asteroids are not great enough to force significant amounts of the volatiles into solution in silicate melts, and so when mantle melting begins in small asteroids, those with diameters significantly less than 100 km, primordial volatiles initially present as a free gas phase largely remain as a free gas phase, and volatiles chemically or physically bound to minerals dissociate into a free gas phase. The resulting pockets of gas can have a wide range of sizes, and in many cases would fill the widths of the veins and dikes through which the melts were rising, separating the liquid phase into discrete batches that would emerge through the surface vents as liquid ribbons separated by the gas pockets, a process called slug flow (Wallis 1969; Ornebere-Iyari et al. 2007). Subsequent hydrodynamic instabilities would lead to the break-up of these liquid ribbons into liquid droplets with a range of sizes, mostly less than approximately 0.3 mm but possibly up to approximately 30 mm in diameter.

The above ranges of pyroclast sizes relate to silicate liquid droplets. We argued above that by the time that the temperature is high enough for a significant amount of silicate melting to have taken place in an asteroid with the composition inferred for the aubrite parent body, Fe,Ni-FeS liquids will also have been formed. These liquids will probably not migrate until a threshold amount of silicate melting occurs, probably at least approximately 20% (McCoy et al. 1997b), and so immiscible mixtures of the two liquids will begin to migrate together. The silicate liquids will be less dense than their mantle host rocks and the Fe,Ni-FeS liquids will be denser than the host minerals, which would suggest that the two liquids should migrate in opposite directions. However, pockets or bubbles of gas trapped within bodies of Fe,Ni-FeS liquid can cause the bulk density of the mixture to be less than that of the host rocks (Keil and Wilson 1993), leading to upward movement of an immiscible mixture of the two liquids

and entrained gas bubbles and pockets. The viscosity of the Fe,Ni-FeS liquid is very much less than that of the silicate liquid, and the consequence (Wilson et al. 2010) is that if only a mixture of Fe,Ni-FeS liquid and gas pockets reaches the surface, most of the droplets into which the Fe,Ni-FeS liquid disrupts are likely to be no more than 5 mm in diameter, and could be much smaller. However, if a three-phase mixture of Fe,Ni-FeS liquid, silicate liquid and gas emerges, the higher viscosity of the silicate liquid is likely to control the disruption process and larger Fe,Ni-FeS liquid droplets are possible.

These new findings about the likely ranges of sizes of pyroclasts on asteroids of various sizes mean that the situation envisaged by Wilson and Keil (1991), in which essentially all the pyroclasts produced on an asteroid of a given size would either be retained on the surface or be ejected into space with more than escape velocity, is an over-simplification. We now understand that for a given combination of values of asteroid diameter, melt volatile content, and melt composition, there will be a critical pyroclast size that marks a boundary: pyroclasts smaller than the critical size will be able to escape completely from the asteroid, but pyroclasts larger than the critical size must eventually fallback onto the surface.

The factors controlling the critical pyroclast size are the asteroid diameter, the molecular weight of the volatile phase, and the mass fraction of the erupted fluid that consists of the volatiles. The way in which the critical size varies with these controlling parameters was computed for silicate pyroclasts by Wilson et al. (2010, their figs. 7 and 8). We have now made the equivalent calculations for hybrid Fe,Ni-FeS-silicate vitrophyre pyroclasts producing composite clasts like those shown in Fig. 1. These calculations require an estimate of the density of such clasts. Based on the dimensions of the composite clast (Fig. 1), we infer that it consists by volume of approximately 40% Fe,Ni-FeS and 60% vitrophyre silicate. The Fe,Ni-FeS component was found earlier to consist of 43 vol% FeNi with density 7900 kg m^{-3} and 57 vol% FeS with density 4570 kg m^{-3} and thus has a mean density of approximately 6000 kg m^{-3}. The vitrophyre component is estimated from the densities of its enstatite-forsterite-diopside-glass constituent minerals to have a mean density of approximately 3200 kg m^{-3}, making the bulk density of the composite clast approximately 4320 kg m^{-3}. Using this value we computed the critical pyroclast diameter as a function of asteroid diameter and mass fraction of volatiles in the erupted fluid shown in Fig. 14.

The horizontal broken line in Fig. 14 marks the approximately 20 mm diameter of the composite clast shown in Fig. 1. The intersections of this line with the curves for various magma volatile mass fractions show
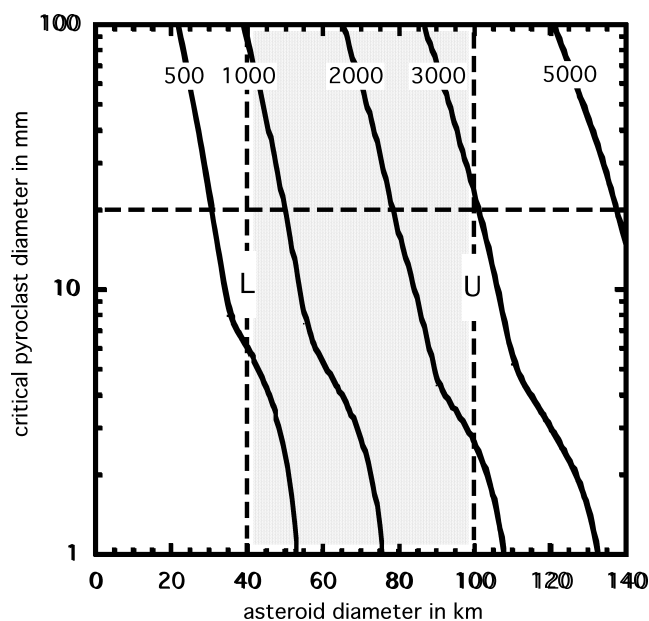

Fig. 14. Variation of critical composite Fe,Ni-FeS-silicate vitrophyre pyroclast diameter with assumed asteroid diameter for a series of values (curves labeled in ppm) of the mass fraction of volatiles with mean molecular mass 40 kg kmol^{-1} that are present in the melt erupting explosively at the surface. Pyroclasts larger than the critical diameter are retained on the asteroid; smaller clasts escape into space. The horizontal broken line presents the clast shown in Fig. 1. The shaded area defines the range of inferred sizes of the aubrite parent asteroid.

the maximum amounts of volatiles that could have been involved in the eruption that produced the clast for a given asteroid diameter; a greater mass fraction of volatiles would have ensured that the clast was ejected with at least the escape speed from the asteroid. To use this information to deduce specific estimates of the amount of volatiles involved we require an estimate of the diameter of the aubrite parent asteroid. There are two potential constraints on this. First, as discussed earlier, explosive eruptions on asteroids larger than approximately 100 km in diameter are not likely to produce pyroclasts larger than a few hundred microns, and so the existence of a clast as large as that shown in Fig. 1 implies that the aubrite parent body was probably less than 100 km in diameter. This upper size limit is indicated by the vertical line labeled U in Fig. 14 and it intersects the horizontal line marking the clast size at a volatile mass fraction close to 3000 ppm, implying that this is likely to be the upper limit to the amount of gas involved. Second, models of the thermal evolution of differentiated asteroids (e.g., Ghosh and McSween 1998; Hevey and Sanders 2006; Sahijpal et al. 2007; Wilson et al. 2008) show that these bodies must

always have a cool outer shell, the thickness of which is at least approximately 10 km, in which conduction to the surface dominates over radiogenic heat production. Thus, unless the asteroid radius is at least of order 20 km, diameter approximately 40 km, it is not likely to attain a significant fraction of silicate melting. This lower limit is shown by the vertical line labeled L in Fig. 14, and implies that the mass fraction of volatiles could have been as small as approximately 700 ppm while still allowing the clast to be retained on a body of this size.

Figure 14 assumes that the mean molecular mass of the volatile phase is 40 kg kmol^{-1}, the value adopted by Wilson et al. (2010) as a plausible average of values corresponding to volatiles likely to be present in a range of compositions of parent asteroids. However, the present work focuses on the aubrite parent body. Muenow et al. (1992) measured indigenous volatiles released at temperatures > 1200 K from enstatite chondrites as a proxy for the parent lithologies of the aubrite meteorites. After minimizing contributions from terrestrial contamination, they found CO (1580–2830 ppm), N_2 (110–430 ppm), Cl (120–450 ppm), and S_2 (possibly up to at least 10,000 ppm). Some of these volatiles may have been trapped in pore spaces and cracks from the time of asteroid formation, whereas others may have been produced by thermal decomposition or chemical reactions, but both types would have contributed to explosive volcanism. The molecular masses (approximately 28, 28, 35 and 64 kg kmol^{-1} for CO, N_2, Cl, and S_2, respectively) and amounts of these volatiles suggest that the mean molecular mass of 40 kg kmol^{-1} used by Wilson et al. (2010) is still a reasonable approximation. However, to give an idea of the consequences of the uncertainty in the volatile composition, we have carried out the same calculations using the likely extreme molecular masses of 28 and 64 kg kmol^{-1}. Figure 15 shows these results, together with values taken from Fig. 14 for a molecular mass of 40 kg kmol^{-1}, and gives the maximum gas mass fraction that allows retention of the composite clast as a function of asteroid diameter. Inserting the same lower and upper limits on asteroid size, 40 and 100 km (the vertical lines in Fig. 15), shows that the maximum range of allowed volatile mass fractions is now somewhat extended and lies between 500 and approximately 4500 ppm.

The above analysis is of necessity based on the single potential large pyroclast so far recognized. It is, of course, possible that larger pyroclasts were retained on the aubrite parent body. Note, however, that the steepness of the solid lines in Fig. 14 means that even if a much larger clast were discovered it would not change the inferred gas mass fraction dramatically. Thus, even if a fivefold larger clast, with diameter approximately 100 mm, were found, the estimate of the lower limit
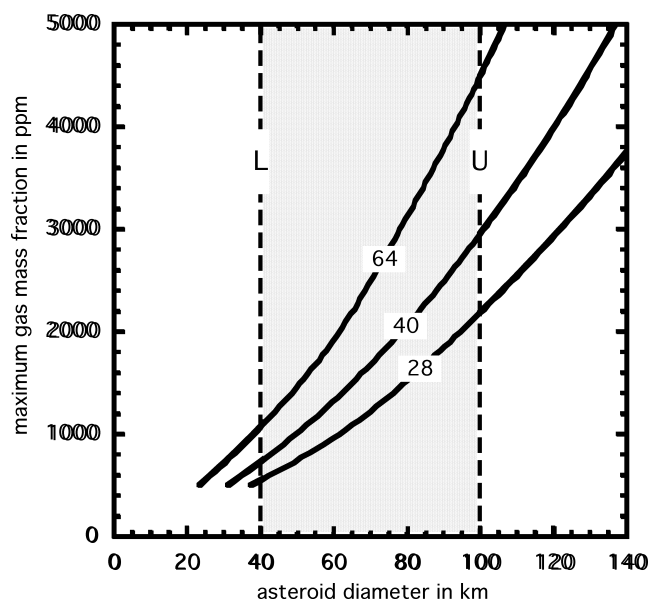

Fig. 15. Maximum gas mass fraction that allows a 20 mm diameter composite Fe,Ni-FeS-silicate vitrophyre pyroclast to be retained on an asteroid of a given diameter for three values of the mean molecular mass (curves labeled in kg kmol^{-1}) spanning the likely range expected for the volatiles driving the explosive volcanism. The shaded area defines the range of inferred sizes of the aubrite parent asteroid.

on the gas mass fraction would increase by only 60% to approximately 800 ppm and the upper limit would increase even less, by approximately 10% to approximately 5000 ppm.

Finally, we comment that there is no way of narrowing the above ranges of volatile content and asteroid diameter without additional information. However, since a 2.5-fold change in assumed asteroid size, from 40 to 100 km, corresponds to an approximately ninefold change in implied volatile content, it follows that a small improvement in knowledge of the asteroid size would yield a large improvement in the volatile content estimate, and vice versa.

Pyroclasts Crystallized and Were Quenched from Relatively High Degree Partial Melts

Although the oxygen isotopic composition of the vitrophyre LAR 04316,4 lies within the lowest range of EH chondrite compositions reported by Newton et al. (2000) and Miura et al. (2007) (Fig. 4), it clearly indicates that the parent lithology of the rock was related to the enstatite meteorite clan. Thus, the parent lithology from which the vitrophyre and, by implication, the Fe,Ni-FeS lithology, formed by partial melting was enstatite chondrite-like. However, considerable evidence has been accumulated that aubrites did not form from

known EH or EL chondrites on their parent bodies (Keil 1989, 2010). We speculate that the enstatite inclusion with metallic Fe,Ni-troilite-keilite globules present within the vitrophyre (Figs. 12A, 13A and 13B) and cut by a vein of vitrophyre interstitial melt (Figs. 12A and 12B) may, in fact, be a xenolith of the partially melted parent lithology from which the aubrites formed by melting and differentiation. We suggest that this "wall-rock material" was engulfed in the Fe,Ni-FeS/vitrophyre melt and retained during pyroclastic volcanism. Supporting evidence for this comes from the Fs content of enstatite of this xenolith (Fs$_{0.33}$; Table 2), which is FeO-poor compared with the enstatite composition in the vitrophyre (Fs$_{2.37}$; Table 2), but more similar to that in the aubrite host (Fs$_{0.07}$; Table 2).

The compositions of the Fe,Ni-FeS and vitrophyre lithologies allow estimation of the extraction temperatures of the partial melts from which they crystallized and, thus, of the degree of partial melting. We determined the composition of the Fe,Ni-FeS lithology to be 56.6 wt% Fe and 43.4 wt% FeS. The Fe-S phase diagram (Kubaschewski 1982) shows that partial melting in the Fe-FeS system begins at 988 °C, and the eutectic melt has the composition of 86.6 wt% FeS and 13.4 wt% Fe. Clearly, the Fe,Ni-FeS clast is not of eutectic composition. As melting proceeds, the eutectic melt will retain this composition until all FeS has melted. With increasing temperature, the amount of Fe in the melt will increase. Thus, the extraction temperature of the Fe,Ni-FeS melt can be read off from the phase diagram for the modal composition of the lithology and gives a value of approximately 1380 °C (we ignore herein the Ni content of the metal and the trace element contents of the FeS).

Based on the composition of the Fe,Ni-FeS lithology, we can speculate on the degree of partial melting that is required to produce the metallic Fe,Ni and FeS in the proportions present in the lithology. If we assume that the Fe,Ni and troilite contents of the parent lithology of the aubrites was anything like the approximate average for H and L enstatite chondrites (which is speculative) of approximately 20 wt% metallic Fe,Ni and approximately 8 wt% FeS (i.e., ratio of metal to troilite approximately 2.5) (Keil 1968), then the ratio of Fe,Ni and FeS in the clast of approximately 1.26 suggests that it represents an approximately 50% partial melt of average EH/EL chondrites.

In Fig. 16, we have plotted the normalized bulk and glass compositions (Table 7) of the vitrophyre lithology in LAR 04316 (subsample "18") in the phase diagram for the system forsterite-albite-silica, following the custom of Fogel (2005). The bulk compositions of enstatite chondrites lie along the enstatite-albite cord and, roughly, so does the bulk composition of the LAR 04316 vitrophyre, but somewhat displaced into the forsterite field. The bulk composition of the vitrophyre falls approximately on the
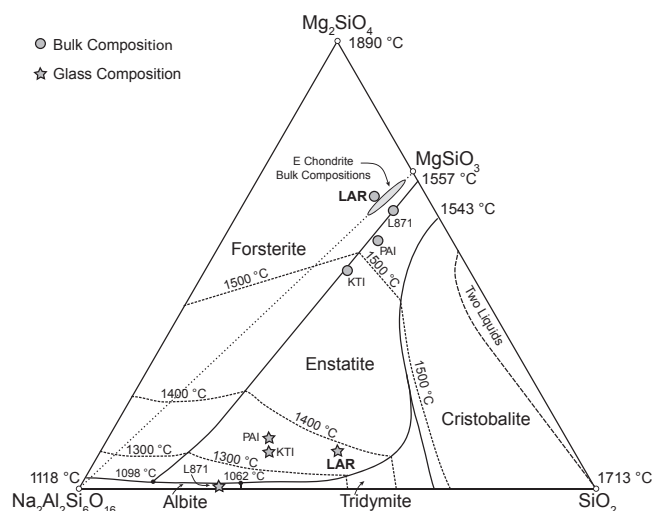

Fig. 16. Phase diagram for the system forsterite-albite-silica, modified from Fogel (2005), and reprinted with permission from Elsevier. Enstatite chondrite bulk compositions lie along the enstatite-albite cord and, roughly, so does the normalized bulk composition of the LAR 04316 vitrophyre lithology (subsample "18"), but somewhat displaced into the forsterite field (filled circle, named LAR). It approximately falls onto the 1535 °C isotherm. The normalized composition of the interstitial glass of the vitrophyre lithology (star, named LAR) lies close to the 1400 °C isotherm, displaced into the enstatite field away from the enstatite-forsterite reaction boundary. The bulk compositions of the ABVs of Fogel (2005) are indicated by three filled circles and their glass compositions by three stars. Data from Table 7.

1535 °C isotherm, which implies that the liquid from which the vitrophyre crystallized was extracted from the parent lithology at approximately 1535 °C. In comparison, the liquids from which Fogel's (2005) aubrite basalt vitrophyres crystallized were extracted at 1485 °C for clast KT1, at 1515 °C for clast PA1, and at 1535 °C for clast L871. Thus, within error, the LAR 04316 vitrophyre partial melt was extracted at approximately the same temperature from its source lithology as was the liquid from which Fogel's (2005) clast L871 crystallized. This is not all that surprising, given that the LAR 04316 clast and L871 most closely resemble each other compositionally. The partial melting experiments of McCoy et al. (1999) on the Indarch EH4 enstatite chondrite provide some guidance in regard to the partial melting behavior of an enstatite chondrite lithology and indicate that partial melting of Indarch is a complex process, having produced three immiscible metallic melts, two immiscible sulfide melts, and a silicate melt. These authors found that silicate partial melting begins at approximately 1000 °C, and Indarch is completely melted at approximately 1500 °C. The metal-sulfide component melts completely at approximately 1000 °C, substantial melt migration occurs at 1300–

1400 °C, and metal migrates out of the silicate charge at approximately 1450 °C and 50% partial melting. Clearly, this high extraction temperature of the vitrophyre liquid implies a relatively high degree of partial melting, but it is difficult to estimate precisely what this degree of partial melting was, because the exact composition of the parent lithology of the vitrophyre, while undoubtedly enstatite chondrite-like, surely was not identical to Indarch. We therefore conclude that the vitrophyre liquid was produced at an exceptionally high degree of partial melting, perhaps approaching complete melting.

The composition of the interstitial glass of the vitrophyre lies near the 1400 °C isotherm, displaced into the enstatite field away from the enstatite-forsterite reaction boundary. The glass composition represents the last composition of the melt before it was quenched, and we therefore conclude that the quench temperature was approximately 1400 °C. This temperature is very close to the extraction temperature of the Fe,Ni-FeS lithology of approximately 1380 °C. Since the Fe,Ni-FeS lithology and the smaller Fe,Ni-FeS objects within the vitrophyre were all quenched at about the same rate, we conclude that the Fe,Ni-FeS and the vitrophyre melts were at a temperature of approximately 1380–1400 °C when they were quenched at a rate of approximately 25–30 °C s^{-1}. For comparison, the quench temperatures for KT1 were 1330 °C, for PA1 1350 °C, and for L871 1070 °C (Fogel 2005).

Editorial Handling—Dr. Ian Franchi

REFERENCES

Barrat J. A., Yamaguchi A., Greenwood R. C., Bohn M., Cotten J., Benoit M., and Franchi I. A. 2007. The Stannern trend eucrites: Contamination of main group eucritic magmas by crustal partial melts. *Geochimica et Cosmochimica Acta* 71:4108–4124.

Benedix G. K., Lauretta D. S., and McCoy T. J. 2005. Thermodynamic constraints on the formation conditions of winonaites and silicate-bearing IAB irons. *Geochimica et Cosmochimica Acta* 69:5129–5138.

Biehl L. and Landgrebe D. 2002. Multispec—A tool for multispectral–hyperspectral image data analysis. *Computers and Geosciences* 28:1153–1159.

Blau P. J. and Goldstein J. I. 1975. Investigation and simulation of metallic spherules from lunar soils. *Geochimica et Cosmochimica Acta* 39:305–324.

Blau P. J., Axon H. J., and Goldstein J. I. 1973. Investigation of the Canyon Diablo metallic spheroids and their relationship to the breakup of the Canyon Diablo meteorite. *Journal of Geophysical Research* 78:363–374.

Bogard D. D., Nyquist L. E., Bansal B. M., Garrison D. H., Wiesmann H., Herzog G. F., Albrecht A. A., Vogt S., and Klein J. 1995. Neutron-capture Cl-36, Ar-36, and Sm-150 in large chondrites: Evidence for high fluences of thermalized neutrons. *Journal of Geophysical Research* 100:9401–9416.

Casanova I., Keil K., and Newsome H. E. 1993. Composition of metal in aubrites: Constraints on core formation. *Geochimica et Cosmochimica Acta* 57:675–682.

Clayton R. N. and Mayeda T. K. 1996. Oxygen isotope studies of achondrites. *Geochimica et Cosmochimica Acta* 60:1999–2017.

Cotten J., Ledez A., Bau M., Caroff M., Maury R. C., Dulski P., Fourcade S., Bohn M., and Brousse R. 1995. Origin of anomalous rare-earth element and yttrium enrichments in subaerially exposed basalts—Evidence from French Polynesia. *Chemical Geology* 119:115–138.

Day J. M. D., Ash R. D., Liu Y., Bellucci J. J., Rumble D. III, McDonough W. F., Walker R. J., and Taylor L. A. 2009. Early formation of evolved asteroidal crust. *Nature* 457:179–182.

Eberhardt P., Geiss J., and Grögler N. 1965. Further evidence on the origin of trapped gases in the meteorite Khor Temiki. *Journal of Geophysical Research* 70:4375–4378.

Eugster O. 2003. Cosmic-ray exposure ages of meteorites and lunar rocks and their significance. *Chemie der Erde-Geochemistry* 63:3–30.

Evensen N. M., Hamilton P. J., and O'Nions R. K. 1978. Rare earth abundances in chondritic meteorites. *Geochimica et Cosmochimica Acta* 42:1199–1212.

Flemings M. C., Poirier D. R., Barone R. V., and Brody H. D. 1970. Microsegregation in iron-based alloys. *Journal of the Iron & Steel Institute* 208:371–381.

Floss C. and Crozaz G. 1993. Heterogeneous REE patterns in oldhamite from aubrites—Their nature and origin. *Geochimica et Cosmochimica Acta* 57:4039–4057.

Fogel R. 2005. Aubrite basalt vitrophyres: The missing basaltic component and high-sulfur silicate melts. *Geochimica et Cosmochimica Acta* 69:1633–1648.

Fogel R. A. and Rutherford M. J. 1995. Magmatic volatiles in primitive lunar glasses: I. FTIR and EPMA analyses of Apollo 15 green and yellow glasses and revision of the volatile-assisted fire-fountain theory. *Geochimica et Cosmochimica Acta* 59:201–216.

Fogel R. A., Weisberg M. K., and Prinz M. 1996. The solubility of CaS in aubrite silicate melts (abstract). 27th Lunar and Planetary Science Conference. pp. 371–372.

Gerling E. K. and Levskii L. K. 1956. Origin of inert gases in stony meteorites. *Geochemistry (International)* 7:707–712.

Ghosh A. and McSween H. Y. 1998. A thermal model for the differentiation of asteroid 4 Vesta, based on radiogenic heating. *Icarus* 134:187–206.

Graf T., Signer P., Wieler R., Herpers U., Sarafin R., Vogt S., Fieni S., Pellas P., Bonani G., Suter M., and Wölfli W. 1990. Cosmogenic nuclides and nuclear tracks in the chondrite Knyahinya. *Geochimica et Cosmochimica Acta* 54:2511–2520.

Greenwood R. C., Franchi I. A., Jambon A., and Buchanan P. C. 2005. Widespread magma oceans on asteroidal bodies. *Nature* 435:916–918.

Heber V. S., Wieler R., Baur H., Olinger C., Friedmann T. A., and Burnett D. A. 2009. Noble gas composition of the solar wind as collected by the Genesis mission. *Geochimica et Cosmochimica Acta* 73:7414–7432.

Hevey P. J. and Sanders I. S. 2006. A model for planetesimals meltdown by ^{26}Al and its implications for meteorite parent bodies. *Meteoritics & Planetary Science* 41:95–106.

Hicks T. L. 2002. Automated mapping and modal analysis of meteorite thin sections using image processing software. M.S. Thesis, University of Hawai'i at Mānoa.

Keil K. 1968. Mineralogical and chemical relationships among enstatite chondrites. *Journal of Geophysical Research* 73:6945–6976.

Keil K. 1989. Enstatite meteorites and their parent bodies. *Meteoritics* 24:195–208.

Keil K. 2007. Occurrence and origin of keilite, $(Fe_{>0.5}, Mg_{<0.5})S$, in enstatite chondrite impact-melt rocks and impact-melt breccias. *Chemie der Erde-Geochemistry* 67:37–54.

Keil K. 2010. Enstatite achondrite meteorites (aubrites) and the histories of their asteroidal parent bodies. *Chemie der Erde-Geochemistry* 70: 295–317.

Keil K. and Wilson L. 1993. Explosive volcanism and the compositions of cores of differentiated asteroids. *Earth and Planetary Science Letters* 117:111–124.

Keil K., Stöffler D., Love S. G., and Scott E. R. D. 1997. Constraints on the role of impact heating and melting in asteroids. *Meteoritics & Planetary Science* 32:349–363.

Kubaschewski O. 1982. *Iron—Binary phase diagrams*. New York: Springer, 185 pp.

Leya I. and Masarik J. 2009. Cosmogenic nuclides in stony meteorites revisited. *Meteoritics & Planetary Science* 44:1061–1086.

Lodders K. 1996. An experimental and theoretical study of rare-earth-element partitioning between sulfides (FeS, CaS) and silicate and applications to enstatite achondrites. *Meteoritics & Planetary Science* 31:749–766.

Lorenzetti S., Eugster O., Busemann H., Marti K., Burbine T. H., and McCoy T. J. 2003. History and origin of aubrites. *Geochimica et Cosmochimica Acta* 67:557–571.

Maloy A. K. and Treiman A. H. 2007. Evaluation of image classification routines for determining modal mineralogy of rocks from X-ray maps. *American Mineralogist* 92:1781–1788.

Mason B. 1966. The enstatite chondrites. *Geochimica et Cosmochimica Acta* 30:23–39.

McCoy T. J. and Gale A. 2006. Pyroclastic volcanism on the aubrite parent body: Evidence from an Fe,Ni-FeS clast in LAR 04316 (abstract). *Meteoritics & Planetary Science* 41:A119.

McCoy T. G., Keil K., Clayton R. N., Mayeda T. K., Bogard D. D., Garrison D. H., and Wieler R. 1997a. A petrologic and isotopic study of lodranites: Evidence for early formation as partial melt residues from heterogeneous precursors. *Geochimica et Cosmochimica Acta* 61:623–637.

McCoy T. G., Keil K., Muenow D. W., and Wilson L. 1997b. Partial melting and melt migration in the acapulcoite-lodranite parent body. *Geochimica et Cosmochimica Acta* 61:639–650.

McCoy T. J., Dickinson T. L., and Lofgren G. E. 1999. Partial melting of the Indarch (EH4) meteorite: A textural, chemical and phase relations view of melting and melt migration. *Meteoritics & Planetary Science* 34:735–746.

Miura Y. N., Hidaka H., Nishizuma K., and Kusakabe M. 2007. Noble gas and oxygen isotope studies of aubrites: A clue to origin and histories. *Geochimica et Cosmochimica Acta* 71:251–270.

Muenow D. W., Keil K., and Wilson L. 1992. High-temperature mass-spectrometric degassing of enstatite chondrites—Implications for pyroclastic volcanism on the aubrite parent body. *Geochimica et Cosmochimica Acta* 56:4267–4280.

Nehru C. E., Prinz M., Weisberg M. K., and Delaney J. S. 1984. Parsa: An unequilibrated enstatite chondrite (UEC) with an aubrite-like impact melt clast (abstract). 15th Lunar and Planetary Science Conference. pp. 597–598.

Newton J., Franchi I. A., and Pillinger C. T. 2000. The oxygen-isotopic record in enstatite meteorites. *Meteoritics & Planetary Science* 35:689–698.

Ornebere-Iyari N. K., Azzopardi B. J., and Ladam Y. 2007. Two-phase flow patterns in large diameter vertical pipes at high pressures. *American Institute of Chemical Engineers Journal* 53:2493–2504.

Rugel G., Faestermann T., Knie K., Korschinek G., Poutivtsev M., Schumann D., Kivel H, Guenther-Leopold I., Weinreich R., and Wohlmuther M. 2009. New measurement of the ^{60}Fe half-life. *Physical Review Letters* 103: 072502. 4 p.

Rumble D. and Hoering T. C. 1994. Analysis of oxygen and sulfur isotopes ratios in oxide and sulfide minerals by spot heating with a carbon dioxide laser in a fluorine atmosphere. *Accounts of Chemical Research* 27:237–241.

Rumble D., Farquhar J., Young E. D., and Christensen C. P. 1997. In situ oxygen isotope analysis with an excimer laser using F-2 and BrF5 reagents and O-2 gas as analyte. *Geochimica et Cosmochimica Acta* 61:4229–4234.

Rumble D., Miller M. F., Franchi I. A., and Greenwood R. C. 2007. Oxygen three-isotope fractionation lines in terrestrial silicate minerals: An inter-laboratory comparison of hydrothermal quartz and eclogitic garnet. *Geochimica et Cosmochimica Acta* 71:3592–3600.

Sahijpal S., Soni P., and Gupta G. 2007. Numerical simulation of the differentiation of accreting planetesimals with ^{26}Al and ^{60}Fe as the heat sources. *Meteoritics & Planetary Science* 42:1529–1548.

Sato M. 1979. The driving mechanism of lunar pyroclastic eruptions inferred from the oxygen fugacity behavior of Apollo 17 orange glass. Proceedings, 10th Lunar and Planetary Science Conference. pp. 311–325.

Scott E. R. D. 1982. Origin of rapidly solidified metal-troilite grains in chondrites and iron meteorites. *Geochimica et Cosmochimica Acta* 46:813–822.

Sharp Z. D. 1990. A laser-based microanalytical method for the in-situ determination of oxygen isotope ratios of silicates and oxides. *Geochimica et Cosmochimica Acta* 54:1353–1357.

Shimizu M., Yoshida H., and Mandarino J. A. 2002. The new mineral species keilite, (Fe,Mg)S, the iron-dominant analogue of niningerite. *Canadian Mineralogist* 40:1687–1692.

Skinner B. J. and Luce F. D. 1971. Solid solutions of the type (Ca,Mg,Mn,Fe)S and their use as geothermometers for the enstatite chondrites. *American Mineralogist* 56:1269–1296.

Smith B. A. and Goldstein J. I. 1977. The metallic microstructures and thermal histories of severely reheated chondrites. *Geochimica et Cosmochimica Acta* 41:1061–1072.

Sparks R. S. J. 1978. The dynamics of bubble formation and growth in magmas: A review and analysis. *Journal of Volcanology and Geothermal Research* 3:1–37.

Taylor G. J. 1992. Core formation in asteroids. *Journal of Geophysical Research* 97:14717–14726.

Valley J. W., Kitchen N. E., Kohn M. J., Niendorf C. R., and Spicuzza M. J. 1995. UWG-2, a garnet standard for oxygen isotope ratios: Strategies for high precision and accuracy with laser heating. *Geochimica et Cosmochimica Acta* 59:5223–5231.

Van Niekerk D., Goodrich C. A., Taylor G. J., and Keil K. 2007. Characterization of the lithological contact in the shergottite Elephant Morraine A79001—A record of igneous differentiation processes on Mars. *Meteoritics & Planetary Science* 42:1751–1762.

Wallis G. B. 1969. *One-dimensional two-phase flow*. New York: McGraw-Hill. 480 p.

Watters T. R. and Prinz M. 1979. Aubrites: Their origin and relationship to enstatite chondrites. Proceedings, 10th Lunar and Planetary Science Conference. pp. 1073–1093.

Weitz C. M., Rutherford M. J., and Head J. W. 1997. Oxidation states and ascent history of the Apollo 17 volcanic beads as inferred from metal-glass equilibria. *Geochimica et Cosmochimica Acta* 61:2765–2775.

Welten K. C., Nishiizumi K., Caffee M. W., Hillegonds D. J., Johnson J. A., Jull A. J. T., Wieler R., and Folco L. 2006. Terrestrial age, pairing and concentration mechanism of Antarctic chondrites from Frontier Mountain, northern Victoria Land. *Meteoritics & Planetary Science* 41:1081–1094.

Wieler R. 2002. Cosmic-ray-produced noble gases in meteorites. In *Noble Gases*, edited by Porcelli D. P., Ballentine C. J., and Wieler R. Reviews in Mineralogy and Geochemistry, vol. 47. Washington, D.C.: Mineralogical Society of America. pp. 125–170.

Wieler R., Baur H., Pedroni A., Signer P., and Pellas P. 1989. Exposure history of the regolithic chondrite Fayetteville. I—Solar-gas-rich matrix. *Geochimica et Cosmochimica Acta* 53:1441–1448.

Wilson L. and Head J. W. 1981. Ascent and eruption of basaltic magma on the Earth and Moon. *Journal of Geophysical Research* 86:2971–3001.

Wilson L. and Keil K. 1991. Consequences of explosive eruptions on small solar system bodies: The case of the missing basalts on the aubrite parent body. *Earth and Planetary Science Letters* 104:505–512.

Wilson L. and Keil K. 1996. Clast sizes of ejecta from explosive eruptions on asteroids: Implications for the fate of the basaltic products of differentiation. *Earth and Planetary Science Letters* 140:191–200.

Wilson L., Goodrich C. A., and Van Orman J. A. 2008. Thermal evolution and physics of melt extraction on the ureilite parent body. *Geochimica et Cosmochimica Acta* 72:6154–6176.

Wilson L., Keil K., and McCoy T. J. 2010. Pyroclast loss or retention during explosive volcanism on asteroids: Influence of asteroid size and gas content of melt. *Meteoritics & Planetary Science* 45:1284–1301.

Wolf R., Ebihara E., Richter G. R., and Anders A. 1983. Aubrites and diogenites: Trace element clues to their origin. *Geochimica et Cosmochimica Acta* 47:2257–2270.